



Design and development of an endoscopic robotic system and deep reinforcement learning path planning algorithm for fine needle aspiration of liver lesions

Raghav Khanna

Project dissertation in partial fulfilment for the degree of
Masters in Healthcare Technologies, 2025

Submitted to the School of Biomedical Engineering and Imaging Sciences
King's College London, United Kingdom

Under the guidance and supervision of
Dr. -Ing. Nikola Fischer MSc BEng
Zhenting Du MRes

29th August 2025

Acknowledgement

I would like to acknowledge and give my warmest thanks to Dr.-Ing Nikola Fischer and Zhenting Du for their continuous support and guidance. Their support carried me throughout these eight months we have spent on this project. I would like to thank my friends and colleagues in this degree, who have been great company during the long hours we spent in EW3. I would like to extend my gratitude to Professor Prokar Dasgupta OBE, whose mentorship throughout my years at medical school and during this degree has been invaluable.

Most importantly, I would like to thank my parents, without whom none of this would be possible. I hope to continue my work and achieve new heights to make them proud.

Abstract

This thesis presents the design, development and evaluation of a novel robotic platform for endoscopic ultrasound guided fine needle aspiration and biopsy. The system combines a four degree of freedom (DoF) two segment tendon driven continuum robot endoscope with a two DoF superelastic nickel-titanium bevel tip steerable needle. Needle path planning is performed by a soft-actor critic (SAC) deep reinforcement learning model NeedleNav, generating complete trajectories from an entry point to a deep-seated target lesion while avoiding critical anatomy. This represents one of the first applications of the SAC model to needle path planning. Evaluation of the TDCR in free space demonstrated bending angles and a workspace comparable to clinical gastroscopes. On grid and trajectory based point sampling, the robot demonstrated a Euclidean mean absolute error (MAE) of $\sim 20\text{ mm}$. NeedleNav demonstrated positive results, achieving convergence to an obstacle avoidance trajectory in 2500 training episodes. Steerable needle curvature was augmented by hand-fabricating notches on its distal section. The needle platform was evaluated using a gelatine phantom. The system achieved observable path deflection compared to obstacle-free trajectories for the same target. The MAE and percentage error for obstacle avoidance trajectories was $\sim 22\text{ mm}$ and 18% respectively. Together, these findings suggest the feasibility of our proposed solution, expanding the reach of endoscopic needle interventions in the liver to deep-seated lesions in the right lobe.

1. Introduction

Liver disease is a significant global health burden, accounting for nearly two million annual deaths and 4% of global mortality.¹ Chronic conditions such as liver cirrhosis and carcinoma are the leading causes of liver related mortality.¹ The unifying pathophysiological theme for such conditions (and some acute pathology such as liver abscess) is the development of lesions in hepatic tissue. The underlying mechanisms differ: cirrhotic lesions are driven by the replacement of healthy hepatocytes with fibrotic nodules, carcinoma lesions arise from malignant disease and abscesses are formed by infectious organisms that trigger necrosis and pus collection. In diagnosing and treating these conditions, aspiration/biopsy of a lesion is a key step, providing definitive cytological, histological or microbiological information that imaging alone cannot offer.²

There are several techniques for sampling liver lesions. The most common approach is percutaneous, where a biopsy (16-18G) or aspiration (22-25G) needle is inserted through the abdomen under ultrasound (US) or CT guidance (figure 1a).² In case of obesity, ascites, coagulopathy or altered anatomy, percutaneous procedures are contraindicated and a trans-jugular liver biopsy (TJLB) is indicated as the second line intervention (figure 1b).² A TJLB is performed by an interventional radiologist under fluoroscopic guidance, advancing a catheter from the jugular vein to the hepatic veins. This procedure carries a higher risk of failed/inconclusive biopsy as the tissue samples obtained are often smaller and fragmented.³

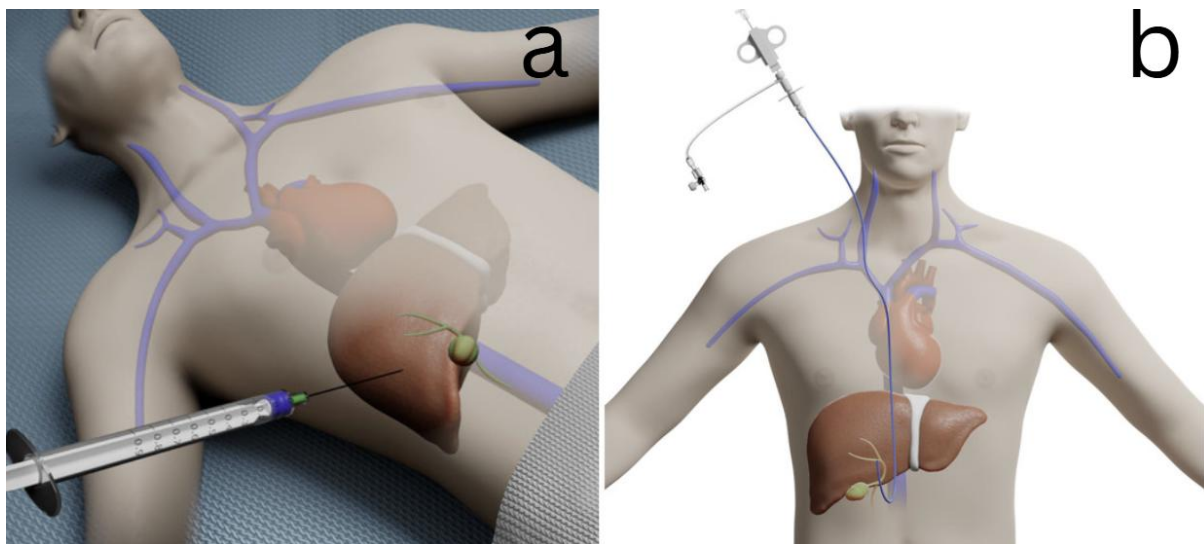


Figure 1: a) percutaneous liver biopsy, b) trans-jugular liver biopsy. Reproduced with permission from [4]

Surgical and laparoscopic biopsies provide larger specimens under direct vision but are invasive, and it is unlikely that a patient who was contraindicated for percutaneous biopsy and TJLB would be fit enough for extensive surgery. In recent years endoscopic ultrasound (EUS) guided techniques have gained prominence as a minimally invasive technique.⁵ EUS fine needle aspiration (FNA) and fine needle biopsy (FNB) target lesions predominantly in the left and caudate lobe of the liver through the gastric or duodenal wall (figure 2).⁵ A US probe is mounted to the distal end of an endoscope, which provides real-time visualization of a straight needle as it punctures the gastrointestinal (GI) wall and reaches the target lesion. Several studies have demonstrated that EUS-FNA and FNB achieve diagnostic yields comparable to those of percutaneous biopsy while maintaining a low complication rate.⁶⁻⁸ This approach, therefore, offers a viable alternative in patients who are otherwise contraindicated for percutaneous procedures.

Despite these advantages, EUS-FNA and FNB have significant technical limitations. Since the needle is straight, lesions that are deep seated, in the right lobe or are adjacent to the bile duct or vasculature are often impossible to sample.⁵ The procedure has a steep learning curve – operators must position the endoscope in a manner that optimizes both the position of needle insertion and a satisfactory US view – and it is thus rarely practiced outside of specialist centres.⁵ These challenges underline the need for a robotic system that integrates an articulable endoscope, steerable needle and autonomous path planning/control for better accuracy, stability, operator ergonomics and ultimately patient outcomes.

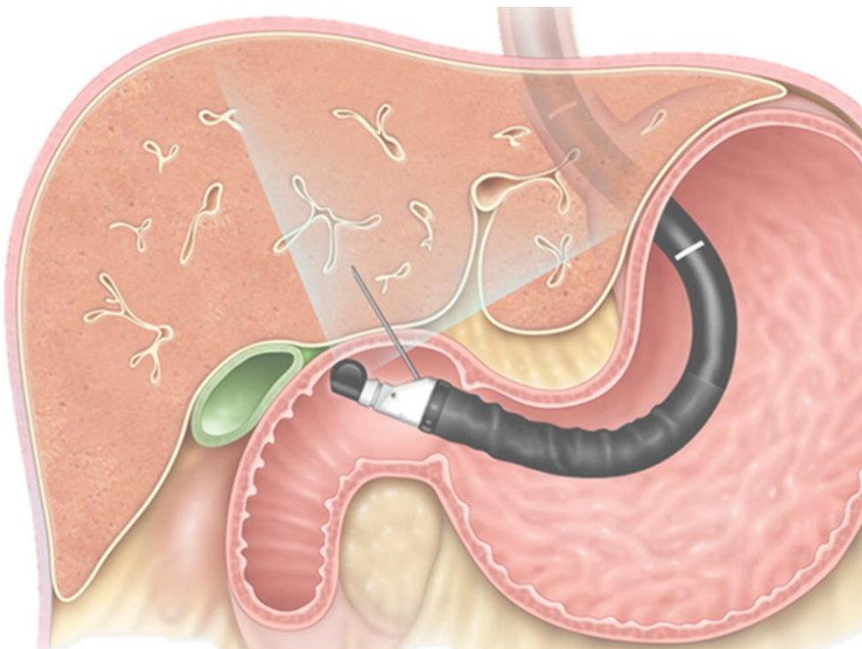


Figure 2: EUS-FNA, illustrating approach to a lesion through the duodenum under US guidance and with a straight needle. Reproduced with permission from [9]

This paper introduces a novel robotic platform of EUS-guided liver aspiration/biopsy, combining a two-segment tendon driven continuum robot (TDCR) endoscope (see section 2) with a super elastic steerable 25G Nickel-Titanium (NiTi) bevel tip needle. Needle trajectory within the liver is generated by a soft actor critic (SAC) deep reinforcement learning (DRL) algorithm. The needle acts as a guidewire and can be used in aspiration, biopsy, ablation and abscess drainage by passing a procedure relevant sheath over it. The objectives of this work are fourfold:

- (a) to design a ‘first stage’ TDCR and control it with inverse kinematics
- (b) to fabricate a ‘second stage’ steerable needle and design its actuation platform
- (c) to implement a DRL path planning algorithm
- (d) evaluate (a) in free space and (b) and (c) in a gelatine liver phantom

To our knowledge, this work represents one of the first integrated evaluations of endoscope, needle and path planner performance in a phantom, and the first application of an SAC to steerable needle path planning for liver interventions.

This paper is arranged as follows: section 2 reviews existing literature on TDCRs, steerable needles and DRL path planners. Section 3 presents the methodology of our work, detailing technical aspects of the first and second stage components of our system. Section 4 reports experimental evaluation of the TDCR and needle. Section 5 discusses findings, limitations and directions for future work.

2. Literature review

Continuum robots (CRs) are a class of highly compliant hyper-redundant robots characterized by a continuous body (as opposed to rigid, serial links).¹⁰ Although the concept of CRs has been described as early as the 1960s, academic work into their implementation in medicine and surgery only began in the early 2000s with advancements in material science, actuation and miniaturisability.¹⁰

While ‘robotic surgery’ has exponentially expanded over the past two decades, this growth has been dominated by laparoscopic soft tissue systems such as the Da Vinci (Intuitive Surgical, California, USA) and hard tissue robots such as the Mako (Stryker Corp., Michigan, USA).¹¹ CRs have a potentially transformative role to play in constrained minimal access procedures (endoscopic, endovascular, transoral/natural orifice surgery) which are largely non-robotic outside a handful of specialized centres worldwide.

CRs can be classified into five types based on their actuation mechanism: tendon driven, concentric tube, multi-backbone, magnetically actuated, intrinsically actuated and steerable needles (Figure 3).¹⁰ An informative paper by Russo et al. (2023) describes each design in detail.¹⁰

2.1. Tendon Driven Continuum Robots

TDCRs are the most prominent class and indeed the design choice for the first stage endoscope in this project. A typical TDCR has a series of discs with a central backbone and peripheral actuating tendons.¹⁰ Segments can be combined in series to create multi-segment TDCRs controlled by tendon triplets terminating at different points throughout the robot. NiTi is a common choice for the fabrication of the backbone and tendons (along with concentric tubes and flexible needles).¹⁰ NiTi also belongs to a family of shape memory alloys (SMA), a property that has been applied in intrinsically actuated continuum robots and articulable tip steerable needles (see section 2.2).

TDCRs have been applied to a wide range of clinical procedures, including neurosurgery, laparoscopy, endoscopy, thoracic surgery and ENT surgery. Kato et al. (2015) presented a two degree of freedom (DoF) single segment TDCR for neuroendoscopic surgery.¹² The design featured a NiTi backbone, three actuating tendons and a tension propagation model to calculate tendon tension loss due to friction, achieving an average tip position error of $5.9 \pm 2.9\text{ mm}$. Kim et al. (2018) proposed MINIR-II, an MRI compatible three segment TDCR for neurosurgery utilising four vertebral discs connected in series by spring backbones and centrally routed tendons for actuation.¹³ The team reported a tip position error of $1.39 \pm 0.54\text{ mm}$. Zhang and colleagues (2018) proposed a three-segment extensible TDCR with concentrically arranged central backbones capable of forward and backward translation

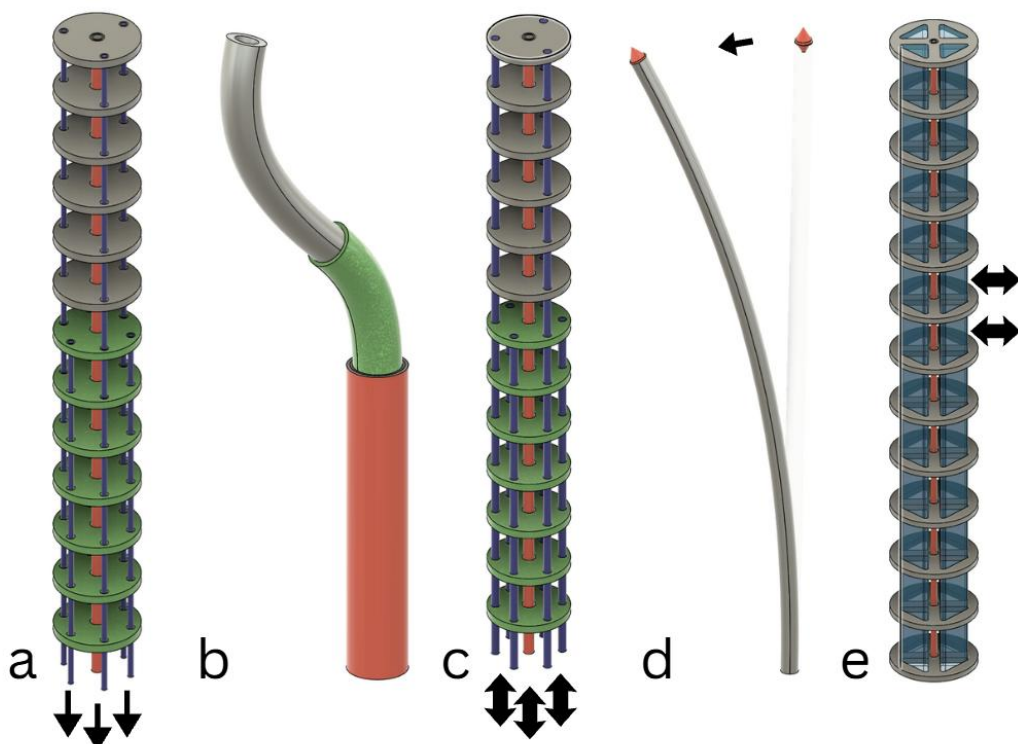


Figure 3: a) Two segment TDCR, b) three tube concentric tube robot, c) multi-backbone continuum robot, d) magnetically actuated continuum robot, e) intrinsically actuated continuum robot.

through the pulling action of four nylon tendons.¹⁴ Experimental evaluation demonstrated a 31% increase in robot length on extension. Dragone et al. (2023) introduced their first prototype of a two DOF neurosurgical TDCR composed of seven uniquely designed vertebrae connected in series to form rolling joints between adjacent segments.¹⁵ Evaluation of the robot in free space demonstrated satisfactory accuracy and repeatability.

Current non-robotic flexible endoscopes apply the same structural principles of tendon actuation but are controlled manually with angulation knobs – roboticization introduces increased accuracy, more DoF, better operator ergonomics and multi-segment architectures. Zhang et al. (2020) presented ten DoF a variable bending section TDCR system for bariatric surgery.¹⁶ A rigid constraint rod was translated into the hollow backbone to vary bending segment length. The continuum component was mounted on a six DoF serial robot and demonstrated adequate flexibility and tracking capability when evaluated in a simulated endoscopic setting. Wang et al. (2021) proposed FIORA, a three segment eight DoF TDCR actuated by 12 NiTi tendons, constructed by combining interlocking male-female discs in series.¹⁷ The device demonstrated a larger workspace compared to the SPORT single port robotic endoscope (Conavi medical, Ontario, Canada) and achieved an average tip position error of 2.3 mm. Amanov et al. (2021) introduced a three segment nine DoF TDCR with extensible concentrically arranged central backbones aimed at minimally invasive surgery (MIS).¹⁸ Magnets were integrated into the vertebrae to ensure equidistant spacing when robot length was varied. The system demonstrated a 22.5% increase in workspace volume and a path following error of 2.59%. Rox et al. (2023) presented a five DoF diameter reducible TDCR with multi-axis foldable vertebrae aimed thoracoscopy.¹⁹ The design made use of hinged vertebrae that closed during insertion through the surgical port and opened on tendon tension. A mean position error of $5.05 \pm 2.64 \text{ mm}$ was achieved on experimental evaluation.

Within ENT surgery, work has focused on transoral and sinus surgery, both of which have an operative field that is highly restricted. Hong et al. (2022) introduced a two segment five DoF TDCR mounted on a serial robot arm aimed at maxillary sinus surgery.²⁰ A novel path following motion strategy was developed for the robot to navigate through the sinus based on a surgeon defined pre-op CT trajectory. In vivo evaluation using a porcine model demonstrated the device's capability to grasp tissue and follow a path accurately. Feng et al. (2022) presented a TDCR end effector for transoral surgery, using a spring central backbone and four actuated tendons for three DoF motion.²¹ The end effector was mounted on a five DoF serial arm and teleoperated by a surgeon on human phantom and porcine models, achieving satisfactory dexterity and exposure of the laryngeal operating region.

TDCRs have been deployed clinically, most notably in form of the Ion (Intuitive Surgical, California, USA) and Monarch (Ethicon, New Jersey, USA) robotic bronchoscopes.²² Additionally, there are tendon driven hyper-redundant highly articulable surgical robots in clinical use, such as the Flex robotic system (MedRobotics, Massachusetts, USA) and instruments of the Da Vinci SP (Intuitive Surgical, California, USA). However, these consist of several discrete vertebrae and are modelled as a long serial chain, not as an elastic curved backbone.²²

Our design choice of a TDCR for the first stage robot was based on their extensive use in the literature for endoscopy and relatively straightforward manufacture, actuation and kinematics. Compared to concentric tube, magnetically actuated and soft continuum robots, TDCRs also have greater stiffness and stability.¹⁰ Multi-backbone continuum robots (MBCRs) are similar in architecture to TDCRs and have been used extensively as endoscopes.¹⁰ However, the use of push-pull secondary backbones (rods) in place of tendons increases diameter and carries the risk of rods deforming when tortuous configurations are repeated.

2.2. Steerable Needles

The second focus of this project is on steerable needles for fine needle aspiration/biopsy. As discussed in section 1, EUS-FNA currently relies on straight needles, making targeting of deep lesions and avoidance of vital structures very challenging. The manual nature of this procedure can cause inaccurate targeting, requiring re-insertions and leading to tissue damage. Interventional radiologists have indicated that there is a clinical need for manipulable needles in liver interventions.²³ Therefore, steerable needles have attracted extensive research attention over the past two decades for use in minimally invasive aspiration, biopsy and ablation.

Generally, four methods for steerability have been explored – active tip articulation, concentric tubes, kinked/curved needle tip and bevel tip.²⁴ Actively articulable designs require the addition of tendons, rods, distal joints or SMAs, increasing diameter and decreasing flexibility. Compliant tips may deflect due to tissue forces when straight insertion is required, increasing error. Concentric tubes are challenging to implement due to their tendency to buckle and snap

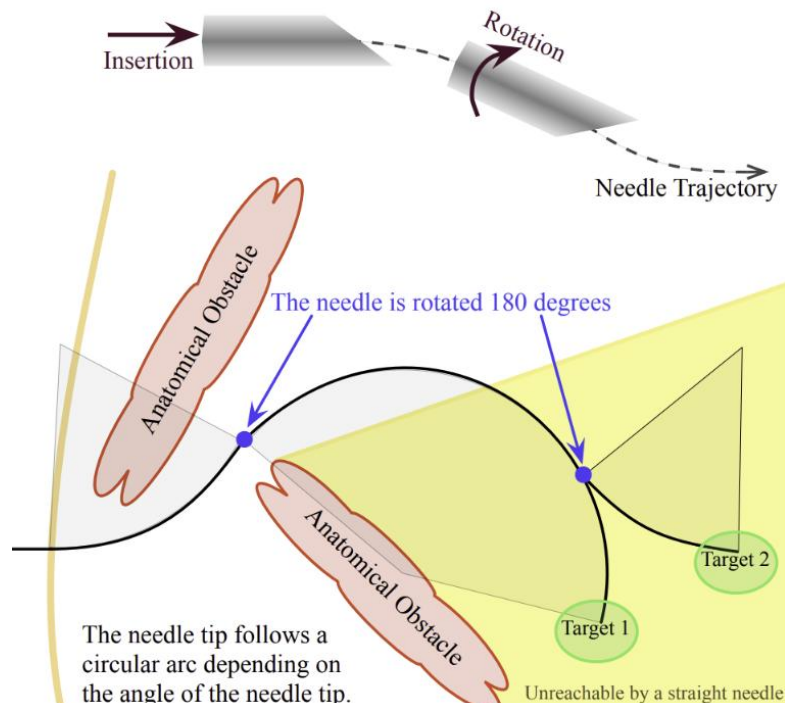


Figure 4: Bevel tip steerable needle navigating through tissue. Reproduced with permission from [27].

through configurations. Kinked needle tips showcase non-uniform bending and cause tissue damage when rotated (ref. section 3.2.1). Rotating kinked needles while initially emerging from the endoscope channel also poses a significant challenge, as the kinked section clashes with the channel walls leading to tip rotational lag. Given these drawbacks, the bevel tip design was chosen as it is simple to fabricate, minimizes damage to surrounding tissue and has a small diameter (0.5 mm, 25G) (Figure 4).

Several bevel tip steerable needle designs have been proposed in the literature. Foundational work by Webster III et al. (2006) evaluated the performance of a 0.7 mm 45° bevel tip needle in ballistic gel muscle phantom (stiffness 4.9 N/mm), modelling it as a non-holonomic vehicle with axial translation and axial rotation as control inputs.²⁵ The authors reported a curvature κ root mean square error (RMSE) of 1.3 mm , demonstrating that the path followed is near-constant curvature and can be steered by axial rotation. Misra et al. (2010) investigated factors that affect κ in tissue by evaluating needles with varied diameter, bevel angle, needle surface in tissue with varying stiffness. The team found that a higher κ can be achieved by increasing bevel angle, reducing needle diameter, increasing needle-tissue friction and using tissue with greater stiffness.²⁶ Reed et al. (2011) evaluated two needles (diameter 0.37 mm and 0.58 mm) with a 45° and 40° bevel tip, augmenting curvature with 12° and 37° pre-bend kink placed 4 mm and 12 mm behind the tip respectively.²⁷ The group noted that placing a kink makes needle behavior non-homogenous, causing a significant lateral tip shift and change in orientation on axial rotation, and addressed this by placing a displacement and orientation offset and compensating for base-tip torsional lag within needle kinematics. Testing in artificial tissue yielded a 3D Euclidean error of $7.9 \pm 1.8\text{ mm}$ and $11.1 \pm 2.5\text{ mm}$ for the 0.37 mm and 0.58 mm diameter needles respectively. Khadem et al. (2018) presented 18G (1.27 mm diameter) 20° bevel stainless steel needles with 0, 1, 2 and 4 sets of five hand-carved notches (depth 0.3 mm , width 0.4 mm , 1.5 mm apart) evaluated in plastisol tissue phantom under ultrasound guidance (ref. section 3).²⁸ The needle was treated as a beam with non-constant cross section and curvature in finite element modelling (FEM) as the notches created a local reduced bending stiffness. The 4 set needle achieved the smallest mean radius of curvature of 205 mm , compared to 616 mm , 452 mm , and 367 mm for the 0, 1 and 2 set needles respectively. Rox et al. (2020) increased the curvature of a 15° bevel tip NiTi needle by laser cutting a helical dovetail pattern along the shaft and machining a flexure hinge (18° hinge stop angle) 10 mm from the tip.²⁹ Evaluation of the needle in bovine liver resulted in $31.3 \times$, $20.3 \times$, and $7.4 \times$ tighter curvatures compared to an unpatterned needle without a hinge, patterned needle without a hinge and an unpatterned needle with a hinge respectively, demonstrating that patterning contributed a larger share of the gain.

2.3. Needle Path Planning

Needle path planning and autonomous control serves two purposes. Firstly, it improves accuracy by reducing reliance on operator skill and the variability this introduces. Secondly, the control policy of bevel tip needles is inherently non-intuitive, making it highly demanding for an operator to understand and evaluate needle motion and action space in real time while

simultaneously avoiding obstacles. Recognising these challenges, a range of path planning techniques have been proposed.

Early work focused on classical approaches such as grid-based search, random tree sampling, potential field gradients, physics-based simulation with FEM and optimisation methods such as particle swarm.^{30,31} These methods are limited by high computational cost, lack of convergence guarantees and the exponentially increasing complexity of the non-holonomic needles as obstacles are introduced.³¹

More recently, classical and DRL techniques have been proposed, offering more efficient path planning, adaptability in a mechanically dynamic environment (to account for nature displacement of tissue) and the ability to introduce hard and soft constraints (e.g. some small blood vessels will get punctured; this is permissible but should be minimised).³¹

Examining the DRL path planning landscape, the general trend is to use a Q value-based model, often variations of a deep Q network (DQN), optimised for discrete action spaces. Lee et al. (2019) developed a DQN for a constant curvature bevel tip steerable needle.³² The model used three fully connected layers with rectified linear unit (ReLU) activations and an RMSprop optimizer. Obstacles were defined on 2D maps of pre-op CT, with a terminal bonus and reward for distance-to-target reduction and a penalty for collision and out-of-bounds movement. To account for non-uniform needle behaviour in tissue, a 10% probability of movement failure was built into the model. Evaluation on CT maps indicated convergence around 2000-2500 episodes with an average success rate of 96.5%.³² Tan et al. (2020) proposed a universal distributional Q learning (UDQL) model for bevel tip needle path planning.³³ Instead of directly predicting discrete actions, the model outputs a distribution of Q values from which the highest-value action is selected. The authors implemented universal value function approximators to enable multi-target planning from the same entry point without retraining. Additionally, prioritised experience replay and hindsight experience replay were implemented in the replay buffer to improve sampling in the presence of rare rewards and accelerate convergence. Hu et al. (2022) presented a path planner for a variable curvature percutaneous liver ablation needle designed around a double deep Q learning network (DDQN).³⁴ 3D segmented reconstructions from pre-op CT were partitioned into voxels with a risk/cost label. The model was first used to sample the skin entry point with shortest path to target from ' n ' candidate paths. It was then trained, given an environment policy that rewarded reaching the target while penalizing vessel and bone collisions and off-directional motion. Simulation based testing generated trajectories that kept larger clearances from vessels and bone compared to a baseline random tree model.³⁴ Lin et al. (2024) presented a 3D path planning DQN built around a composite reward structure and attraction-repulsion potential shaping.³¹ The model has two identical online and target Q networks of three layers with 20 units per layer, ReLU activations and RMSprop optimization. The authors implemented a curvature varying model to simulate bevel tip needle insertion into tissue with differing stiffness. Evaluation in a simulated laparotomy workspace achieved higher rewards compared to a baseline DQN model.³¹

The control policy of steerable needles has both continuous and discrete elements. For instance, in our control policy, the length of insertion can vary between 0 mm and 5 mm, but the choice

between curved or straight trajectories is binary. There is a clear gap in literature regarding continuous algorithms such as actor-critics needle path planning. These reasons form the motivation behind our use of a SAC model.³⁵ SAC handles continuous action spaces well, and continuous outputs for discrete actions can be made discrete via simple thresholding. The nature of SAC (entropy regularized, twin Q critics, discussed in detail in section 3.2.2) also makes future work in tissue and curvature variability modelling feasible.

Having discussed the background literature and motivations behind high-level design choices, the next section presents a detailed technical description of the hardware and software components of the project.

3. Methodology

3.1. First stage: continuum endoscope

3.1.1. Design and actuation

Building on insights from our literature review and objectives, we designed a TDCR that acts as an actively controlled distal section of an endoscope (figure 5c). The bending angles of GI gastroscopes typically fall around 195° upward, 80° downward and 90° laterally.³⁶ Our two-segment design achieves comparable bending with a larger workspace and more DoF. It avoids the mechanical and control complexity of three or more segments. Mounting the TDCR on the endoscope introduces a fifth degree of freedom, which will allow it to reach a commanded position and direction.

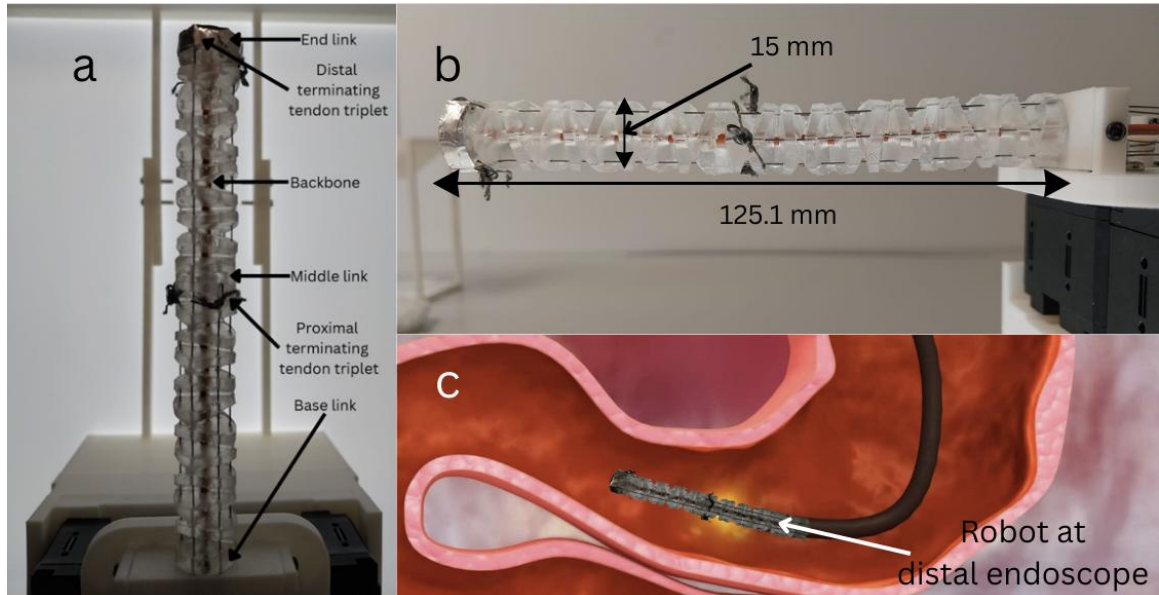


Figure 5: a) Labelled image of the first stage TDCR, b) side view of the TDCR, c) placement of the TDCR on the distal endoscope section.

The core structural body is SLA printed (Form3, Clear Resin, Formlabs) and has an initial base link, ten identical spacer discs arranged perpendicularly to each other, a middle link at which point the first segment terminates, eight spacer discs and an end link (figure 6). Discs are interlocked through male-female mating surfaces to form a series of constrained pivot joints. The male surface features two short, cylindrical protrusions separated by a central bore. The corresponding female surface has a circular depressed slot into which the male protrusions fit neatly. The central bore accommodates the steel spring backbone, repurposed from single wire endoscopic biopsy forceps, and provides key stiffness support to the robot. The discs contain either six (proximal segment) or three (distal segment) peripheral channels for tendon routing. Tendons controlling the proximal segment terminate at the middle link, while tendons controlling the distal segment terminate at the end link. Before entering the robot body, tendons are routed through a base tendon guide that brings them together in a hub-spoke fashion to accommodate their symmetrical antagonistic pairing. Steel bushings are incorporated into the tendon guide to act as durable, low-friction channels.

A TDCR is actuated by tendon tension; in our design, tendons are proximally wound around pulleys mounted on top of six servos, fixed in place by a screw. To accommodate the hub-spoke tendon arrangement, pulley pairs are offset by 3 mm in height and the middle pair is offset by 2 mm laterally (figure 7). Pulleys are attached to the motor horn with M2 screws. The servo motors used are six Dynamixel XL-430 W250Ts chosen for their high stall torque at relatively small power draw (1.5 Nm , $12V$, $1.4A$). The motors use a 12-bit encoder and have a practical physical resolution of 0.2 mm tendon length change for 20 encoder ticks. Servos are connected in a daisy chain to a Dynamixel shield, in turn mounted on an Arduino R4 Uno. An upper and lower plate secure the motors in place using M2.5 screws, offset in the same manner as the pulleys described above. Dimensions of all components above are given in table 1 below.

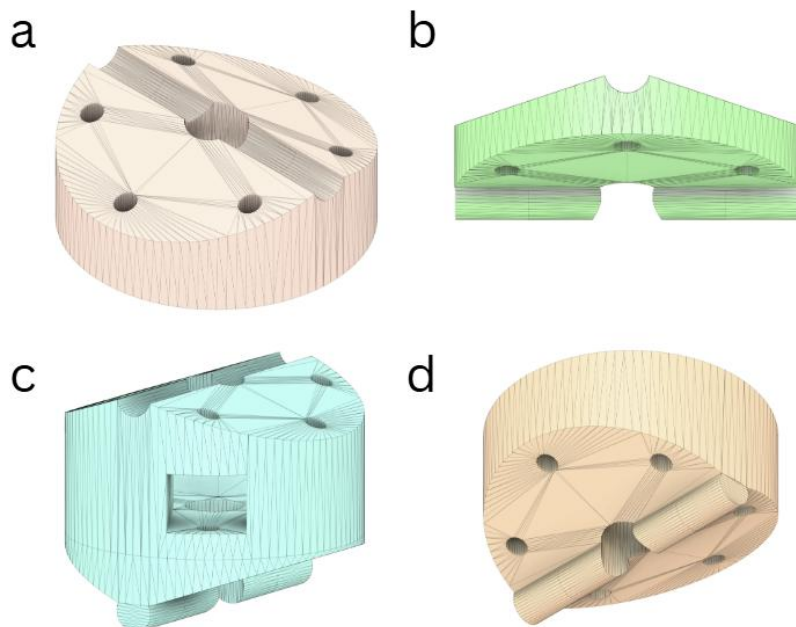


Figure 6: a) Initial base link, b) spacer discs, c) middle link, first segment tendons tied off at the windows, d) end link.

Table 1: Dimensions of important components in the TDCR

Component	Measurement (mm)
TDCR diameter	14
Central channel outer diameter (OD)/inner diameter (ID)	2.3/1.2
Peripheral channel diameter	0.5
Tendon diameter	0.3
Pulley diameter	4.5
Pulley/motor height offset	3
Middle pulley/motor lateral offset	2
Stainless steel needle guide OD/ID	2/1

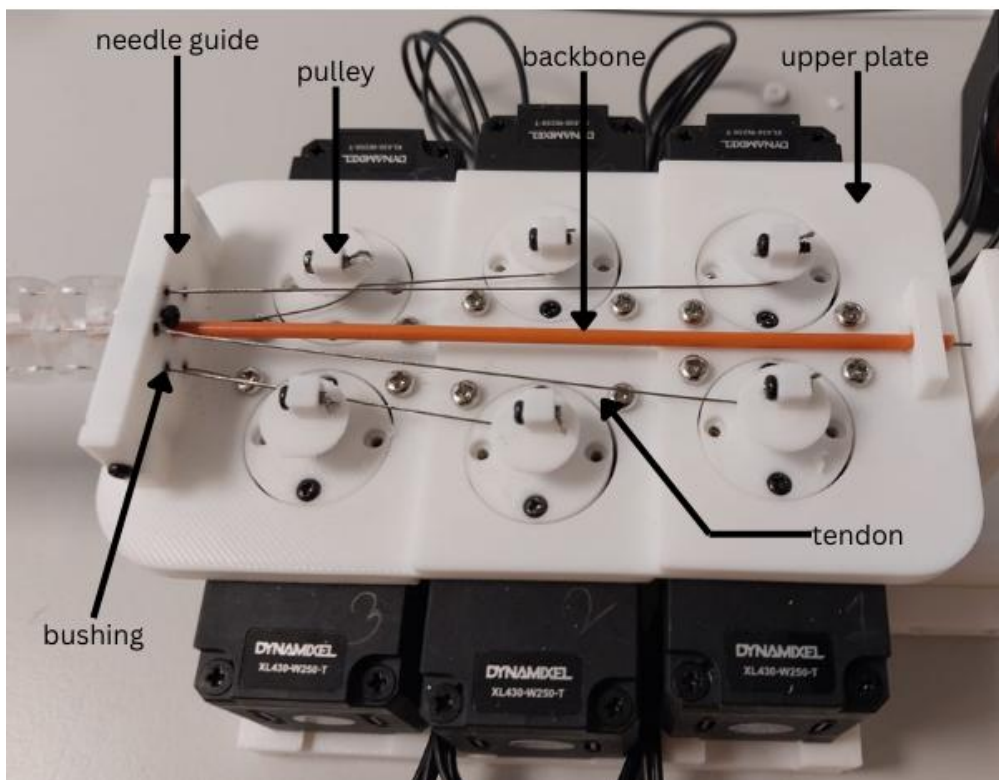


Figure 7: Tendons wound around six pulleys offset posteriorly and laterally. Orange central channel is clearly visible.

3.1.2. Inverse kinematics with FABRIKc

Forward and inverse reaching inverse kinematics for continuum robots (FABRIKc) is an inverse kinematic (IK) framework first proposed by Zhang et al. (2018).³⁷ The model is based on the FABRIK IK solver for serial robots which iteratively moves joints towards a base-link and end-link target through forward and backward passes, gradually converging to a satisfactory configuration. FABRIKc extends this principle to continuum backbones by approximating a constant curvature arc as a virtual link that connects the arc base and tip. In each iteration, parameters of the virtual link are updated, and arc parameters (bending angle, tip and base positions) are adjusted. The forward and backward passes continue until the target error condition is satisfied.

The FABRIKc framework is particularly well suited for this work: it converges to a solution quickly and is computationally inexpensive, avoids complex mathematical operations with pseudoinverse Jacobian and is stable near singularities.³⁷ Jacobian and optimisation-based techniques, variable curvature models and kinematics-statics models are comparatively slower, less stable and computationally demanding, making FABRIKc a more practical choice for this first version of our continuum endoscope.³⁷ A detailed technical description of the IK model is given below.

Before beginning our forward-backward iteration, the initial values for each parameter must be assigned. For an n segment continuum robot, each segment can be assumed as a constant curvature arc. Each section t has an arc length L_t , bending angle, θ_t , bending plane angle δ_t (both initialized as 0 in our implementation), target tip position $p_{e,t}$, target orientation $z_{e,t}$, and base position $p_{b,t}$. We also calculate an initial virtual link length l_t^0 and position $p_{j,t}^0$ based on present θ_t :

$$l_t = r \tan \frac{\theta_t}{2} = \frac{L_t}{\theta_t} \tan \frac{\theta_t}{2} \quad \dots (1)$$

$$p_{j,t}^0 = p_{b,t} + l_t z_{b,t} \quad \dots (2)$$

$$t = 1 \dots n, z_{b,t} = [0,0,1]$$

Backward pass fixes the tip and solves for the base position (figure 8). The virtual joint position $p_{j,t}$ can be calculated as:

$$p_{j,t} = p_{e,t} - l_t z_{e,t} \quad \dots (3)$$

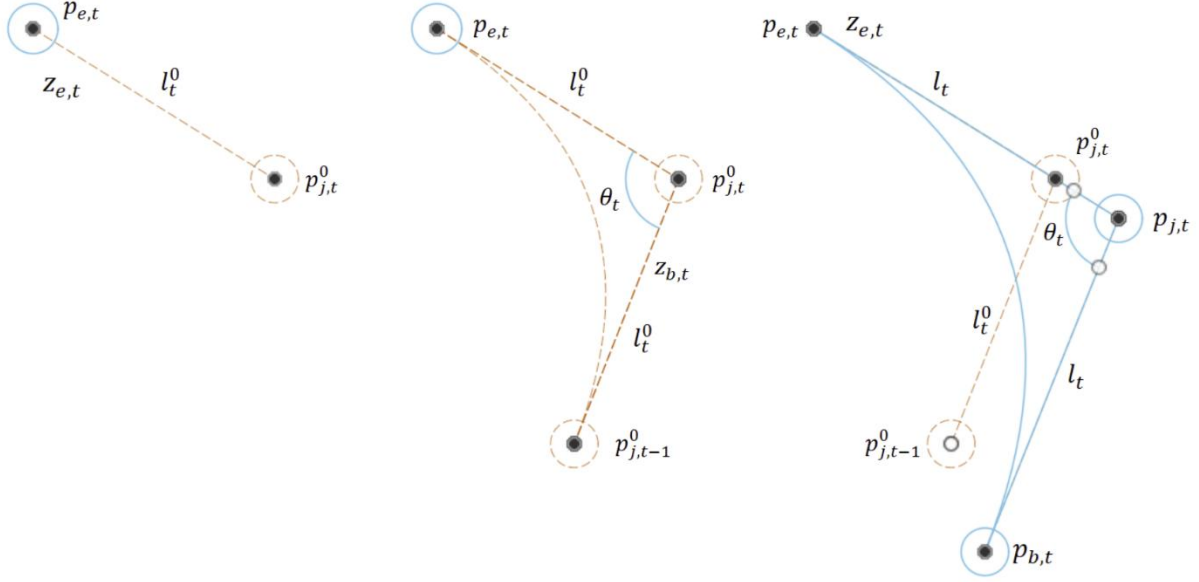


Figure 8: Backward pass of FABRIKc. Detailed diagrams of forward and backward passes over a full three segment TDCR are available at [37]

The base orientation can be calculated by connecting the new virtual joint as above and the old virtual joint for the $t - 1$ th segment:

$$z_{b,t} = \frac{p_{j,t} - p_{j,t-1}^0}{\text{norm}(p_{j,t} - p_{j,t-1}^0)}, t > 1 \quad \dots (4)$$

$$z_{b,t} = [0, 0, 1], \quad t = 1$$

We can now update the bending angle θ_t to reflect the newly assigned $z_{b,t}$:

$$\theta_t = \arccos(z_{b,t} \cdot z_{e,t}) \quad \dots (5)$$

Based on this new value, we can repeat the above equations (1), (3) and (4) to update the values of l_t , $p_{j,t}$ and $z_{b,t}$. Finally, $p_{b,t}$ can be calculated as:

$$p_{b,t} = p_{j,t} - l_t z_{b,t} \quad \dots (6)$$

We have essentially moved ‘backward’, first projecting the initial virtual link length along the target tip orientation, then calculating the segment base orientation unit vector by comparing the positions of the t th segment virtual link and $t - 1$ th segment virtual link. If $t > 1$, then $z_{b,t} = z_{e,t-1}$

The forward pass then fixes the base $p_{b,t}$ and solves for the tip position and orientation $p_{e,t}$ and $z_{e,t}$ (figure 9):

$$z_{b,t} = [0, 0, 1], \quad t = 1$$

$$z_{b,t} = z_{e,t-1}$$

$$p_{b,t} = p_{e,t-1}$$

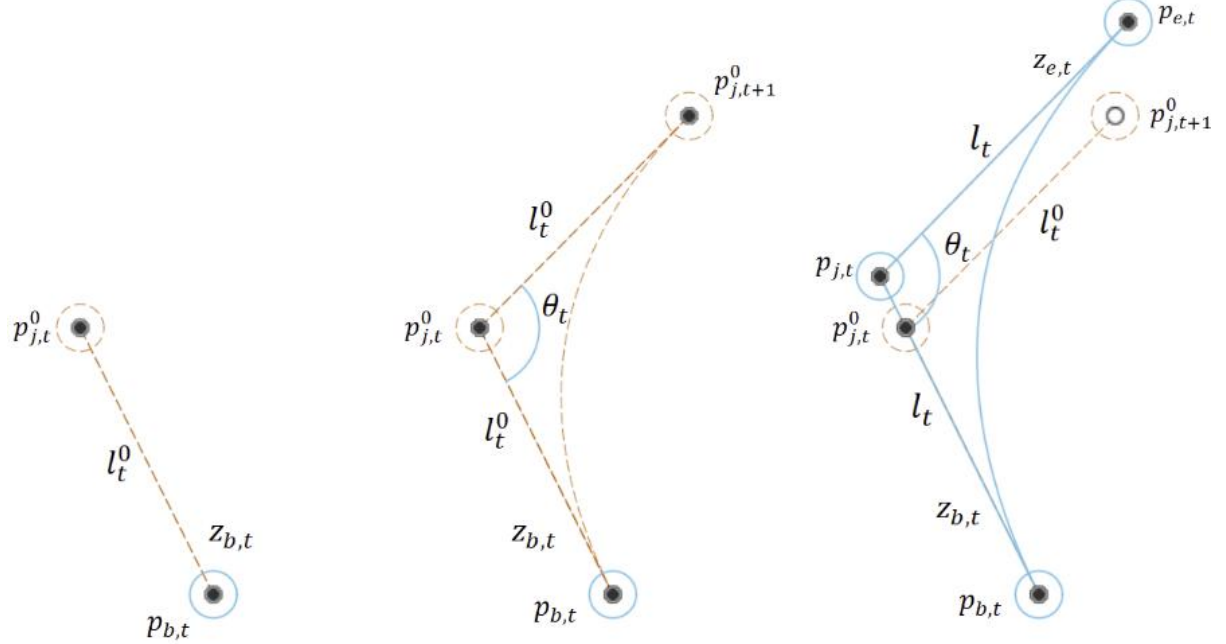


Figure 9: Forward pass of FABRIKc

The first virtual link is placed on $p_{j,t}$ as:

$$p_{j,t} = p_{b,t} + l_t z_{b,t} \quad \dots (7)$$

$z_{e,t}$ is calculated by connecting $p_{j,t}$ and $p_{j,t+1}^0$:

$$z_{e,t} = \frac{p_{j,t+1}^0 - p_{j,t}}{\text{norm}(p_{j,t+1}^0 - p_{j,t})} \quad \dots (8)$$

For $t = n$, $z_{e,t}$ is the target tip orientation. Based on this value, we can update the bending angle θ_t :

$$\theta_t = \arccos(z_{b,t} \cdot z_{e,t})$$

Equations (1), (7) and (8) can be used to update the values of l_t , $p_{j,t}$ and $z_{e,t}$. $p_{e,t}$ is calculated as:

$$p_{e,t} = p_{j,t} + l_t z_{e,t} \quad \dots (9)$$

The position error is calculated as:

$$\varepsilon = p_{target} - p_{e,n}$$

Forward and backward iterations are repeated until the condition $\varepsilon < \varepsilon$ is satisfied. The bending plane angle δ_t is calculated by taking the x and y values of chord between the tip and base and applying *atan2*:

$$\delta_t = \text{atan2}(-y, x)$$

As an important note, satisfying both the target position and orientation requires a 6 DoF system, which makes our first stage endoscope underactuated. Calling FABRIKc in this situation outputs a configuration that satisfies the orientation condition (a hard constraint) and tries to find a best-fit position until $kmax$ (maximum number of iterations) is reached, with some residual position error. Position control only results in a near-perfect tip position achieved on simulation. The real system accuracy for both scenarios has been presented in section 4.

FABRIKc outputs (θ_t and δ_t) need to be translated into tendon lengths and motor inputs for a complete kinematic workflow. A seminal paper by Webster III and Jones (2010) is the basis for our length calculation framework.³⁸ We first begin with an expression for the length of the segment backbone, which is an arc of a circle radius R . The chord length of the backbone is:

$$c = 2R \sin \frac{\theta}{2}$$

If the segment is split into n small arcs ds , then the total length S is approximately equal to the total chord length:

$$S \approx C = 2nR \sin \frac{\theta}{2}$$

However, the length $l_i, i = 1, 2, 3$ for three actuating tendons arranged at angle φ_i around the backbone is not the same as S , since they are radially offset by d (0.3 mm). From Webster III and Jones (2006), we have:

$$l_i = R - d \cos(\delta - \varphi_i)$$

Tendons are arranged at 120° from each other, at $\varphi_1 = 90^\circ$, $\varphi_2 = 210^\circ$, and $\varphi_3 = 330^\circ$.

Having obtained l_i , we can use a simple workflow to obtain exact pulley angular rotation and motor increments. At zero position (straight configuration) $l_i = S$. The change in tendon length in mm is:

$$\Delta l_i = (S - l_i^{new}) * 10$$

Given the pulley diameter and a 12-bit motor (4096 total ticks), we can calculate:

$$motor\ ticks = \frac{4096}{4.5\pi} * abs(\Delta l_i)$$

The lengths of each triplet for both segments can be calculated independently. Thus, we have a complete IK model – given a target tip position and orientation, the necessary raw ticks for all six motors are outputted.

3.2. Second stage: steerable needle

3.2.1. Fabrication and actuation

The steerable needle stage is the core mechanical component that enters the liver and reaches the target lesion. This solid needle has a diameter of 0.5 mm (25G) and is made of super-elastic NiTi. As briefly introduced in section 1, the needle bends due to the asymmetric forces applied on the angled bevel tip (figure 10). This creates a relatively straightforward control policy for two DoF: the needle can be translated forward (without rotation) to bend in tissue or can be translated and simultaneously rotated continuously in a drilling fashion to move straight in tissue. While curvature remains fixed (theoretically; discussed in greater detail in section 4), the bending angle of an arc motion and the plane it bends in can be changed by torsional rotation.

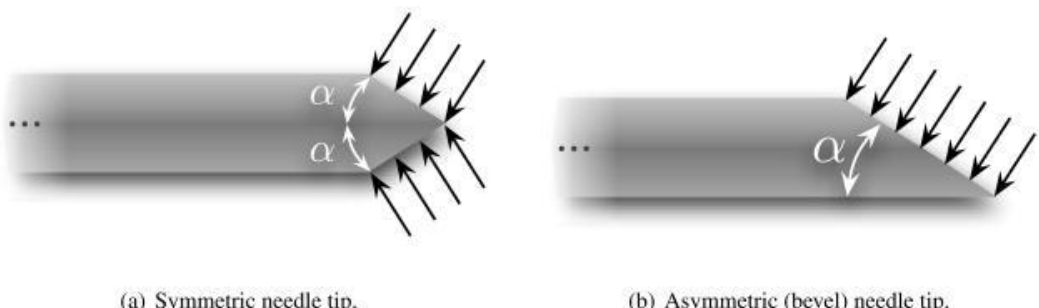


Figure 7: Tip-tissue interaction forces for bevel tip needle. Reproduced with permission from [26]

A bevel tip angle of 26° was fabricated using 2000 grit sandpaper. Initial experimentation in 11.3% w/v Gelatine with only the bevel tip demonstrated a very small deflection. Various strategies to increase curvature were explored, including manually creating a kink close to the tip to increase curvature, offsetting the tip and body by a small gap and combining them with silicone shrink tubing and using NiTi's SMA property to set a local or global curvature. The former two approaches proved to be unstable and caused significant damage to the phantom. The latter strategy is commonly used in NiTi based concentric tubes, however, was unsuitable for our work as straight motion would no longer be possible. Based on designs from Khadem et al. (2018), a satisfactory solution was found in creating deep notches using a diamond file (0.3 mm deep, 0.25 mm apart) on a 3 cm section immediately proximal to the tip, significantly increasing the local curvature of the needle (figure 11). The curvature of the needle was approximated to 10.44 m^{-1} after experimentation. An exact value could not be determined as the curvature is not uniform throughout the needle (the notched section has very high curvature, to the order of 30 m^{-1}) and is dependent on the length and speed of insertion.

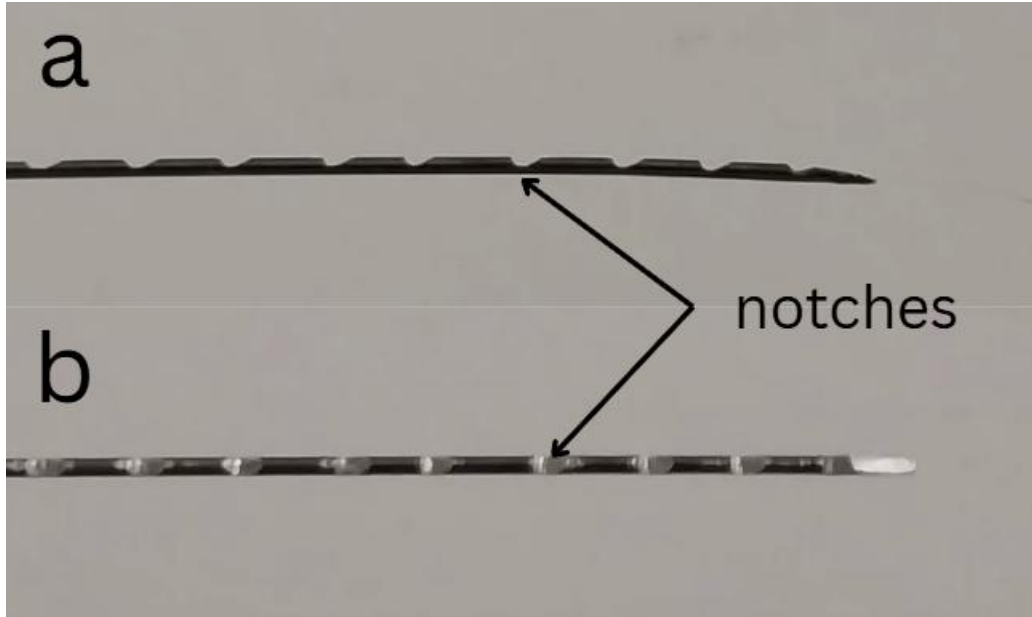


Figure 8: a) Superior and b) lateral view of the notched needle section

Actuation of the needle is based on a 3D printed PLA rack-pinion mechanism (figure 12a). The rack (module = 1 mm, pressure angle = 20 degrees, backlash = 0) is translated forward by a pinion gear (module = 1mm, pressure angle = 20 degrees, backlash = 0, 14 teeth) attached to a Dynamixel XL-330-M288-T servo. At the endoscope facing end of the rack, a second Dynamixel XL-330-M288-T is mounted for rotational motion. These motors were chosen for their high RPM, which is ideal for in-tissue straight motion.

During motion inside the phantom, the non-working length of the needle between the central channel and proximal point attached to the motor was found to buckle significantly. To address this, an accordion style needle guide was created (figure 12b) inspired by the guide system used in the Ion system (Intuitive Surgical, Sunnyvale, California).³⁹ A series of four bar parallelograms with colinear channels were arranged, securing the needle in one axis while allowing free translation and rotation.

The first stage and second stage platforms were fixed together by two pairs of M2.5 screws, creating the complete system as described.

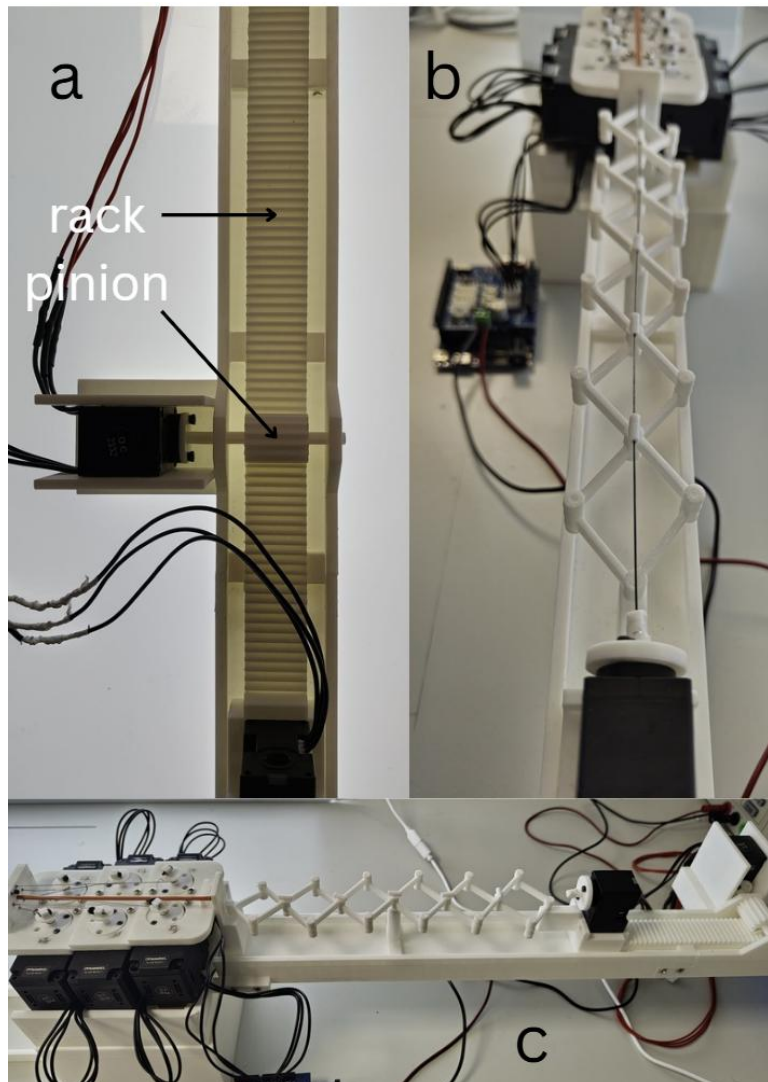


Figure 9: a) rack-pinion mechanism, b) accordion style needle guide,
c) TDCR and needle platforms combined

3.2.2. NeedleNav – deep reinforcement learning based path planning for Needle Navigation

NeedleNav is an online, off-policy DRL path planner built on the soft actor critic (SAC) setup.³⁵ NeedleNav takes in a 9D observational vector (entry position, orientation and target position) and outputs a per-step 3D action vector: length (constrained between 0 and 5 mm), a binary steer command (straight or curved motion) and the bending plane angle (between π and $-\pi$). The algorithm can construct a complete path given a specific needle curvature (in this case, 10.44 m^{-1}) while avoiding obstacles mimicking vascular structures. A SAC works as an antagonistic pair; an actor learns a policy while a critic evaluates the policy and grades the value of an action to move the actor towards better outputs. It also introduces an entropy term that assigns randomness to the policy, promoting exploration in the early stages of training.

All code used is available at <https://github.com/TheLordKhanna/needle>.

In this setup, the actor is a multilayer perceptron (MLP) network with two fully connected hidden layers (256 units + ReLU) that takes in the 9D input vector as above and outputs two 3D vectors: the mean $\mu_\theta(s)$ and log-standard deviation $\log \sigma_\theta(s)$ (figure 13). θ denotes actor weights. These parameters are used to construct a gaussian probability distribution $\mathcal{N}(\mu, \sigma^2)$ (figure 13). $\mathcal{N}(\mu, \sigma^2)$ is randomly sampled by a noise variable ϵ (the reparameterization trick) to obtain a pre-squashed action sample z , given by:

$$z = \mu_\theta(s) + \sigma_\theta(s)\epsilon$$

This is a key step that results in a deterministic, differentiable function of θ and thus gradient optimisation using the Adam optimizer can be performed.

z is then squashed to $[-1, 1]$ by applying tanh, ensuring stable gradients:

$$u = \tanh(z) \quad \dots (9)$$

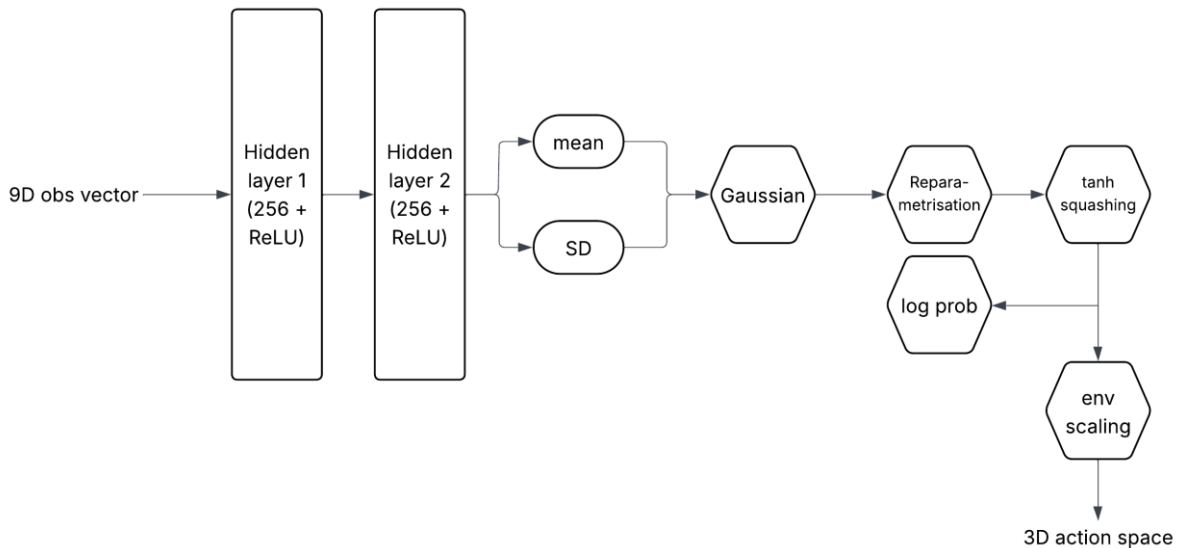


Figure 13: Actor diagram from observation space to action space

u is further scaled in the environment space to obtain the final action vector a :

$$a = g(u)$$

Although not used in the forward pass, this is an appropriate time to introduce the log-probability of u , used in backpropagation for the actor, critic and entropy update, given by:

$$\log \pi_\theta(u|s) = \mathcal{N}(z; \mu, \sigma^2) - \sum_{i=1}^3 \log(1 - \tanh^2 z_i)$$

The log-probability for squashed action u subtracts the gaussian distribution above by the tanh Jacobian to conserve the probability space that has now been warped in equation (9). It measures how typical or expected (low surprisal) the sampled action is for s – larger (less negative) values signify that a fixed policy expects to take similar actions for similar states.

The critic is another fully connected MLP that takes a 12D input (the 9D observation space and the 3D action output by the actor in its first forward propagation) and outputs a single $Q(s, a)$ value. We apply double Q critics in this setup, thus two critics output two independent values Q_1 and Q_2 . Two duplicate target critics Q_1^t and Q_2^t are used as slow-moving copies of the online critics to build a stable target for online critic training.

This concludes the forward propagation step for our SAC. Backpropagation uses the loss to compute gradients for actor, critic and entropy weights. A core concept in this setup is off-policy learning – current weights can be learned using data derived from previous episodes. A five-element tuple containing s, a, r (reward), s' (new state) and d (termination or no termination binary variable) are stored in a replay buffer and random minibatches of size 256 are drawn from that buffer for current policy training. Up to 200,000 tuples of past steps (each episode containing 200 steps) are stored, and oldest steps are removed once the buffer limit is reached.

Thus, for the first step in backpropagation, online critic weights are updated by calculating the mean squared error (MSE) of $Q - y$, where y represents backup, the one-step soft bellman target, given by:

$$\text{backup } (y) = r + (1 - d)\gamma(\min(Q_1^t, Q_2^t)(s', a') - \alpha \log \pi(a'|s'))$$

Where r is the immediate reward for an action that takes a given state s to a new state s' , d is the termination condition (1 if terminated, 0 if not), γ (0.997) is the discount factor scaling the importance of the value of s' , $\min(Q_1^t, Q_2^t)(s', a')$ is the minimum Q value from target critic pair for that s', a' pair calculated by target critic forward propagation, and $\alpha \log \pi(a'|s')$ is the entropy temperature scaled log-probability term for the s', a' pair (equation (4)). This latter term is included to reward entropy – a policy with higher entropy will have a bigger variance, and thus the log-probability will be smaller (higher negative value). $-\alpha \log \pi$ will have a larger positive value and thus y will have a larger value, minimising the critic MSE loss. If a policy

with a large enough Q value is found, the influence of the entropy term is overshadowed, and critic weights β are moved towards the better policy. The MSE error is calculated as:

$$L_{Q_i}(\beta_i) = \mathbb{E}(Q_i(s, a) - y_i)^2, i = 1, 2$$

Where \mathbb{E} denotes that the final L_{Q_i} is the average value from a 256 step Monte Carlo estimate over the replay data. The new value of β is:

$$\beta_{new} = \beta - \eta \frac{\partial L_Q}{\partial \beta} \quad \dots (10)$$

It is important to note that y is calculated using the target critic Q for the next s' , a' , and Q_i are the critic values for the previous s, a – we are moving the critic gradually towards Q values that match y_i . Target critics are not updated with optimisation of loss but are instead brought closer to online critic weights using a Polyak averaging coefficient $\tau = 0.005$.

For actor backpropagation, the goal is to minimize its expected loss, given by

$$L_{actor} = \mathbb{E}(\alpha \log \pi_\theta(u|s) - \min(Q_1, Q_2)(s, g(u)))$$

In simple terms, the actor tries to minimize its loss by choosing actions preferred by critics (large Q values) while preserving some randomness. $\min(Q_1, Q_2)(s, a)$ is obtained by forward propagation through the online critics. At this point, critic weights are frozen. Actor weights θ are updated in the same manner as equation (10).

The entropy ‘temperature’ α is also learned during training to converge on an entropy that balances exploration and exploitation, given by:

$$H(\pi) = -\mathbb{E}(\log \pi(a|s))$$

The policy minimizes:

$$L_\alpha(w) = -w \mathbb{E}(\log \pi_\theta(a|s) + TE)$$

Where $w = \log \alpha$ and TE is the target entropy, assigned $-\dim(action\ space) = -3$ in our setup. If the entropy is too low, $\log \pi_\theta(a|s)$ has a large value, and α increases.

The backpropagation logic above is held in agent.py. Network.py initializes the agent and critic architecture, and buffer.py runs functions to add and randomly sample tuple minibatches.

Table 2: Reward and penalty values for the needle steering environment

Reward/penalty	Assignment in env	Value
Distance reduction reward	<i>distance_weight</i>	150
In sphere one-off bonus	On reaching <i>switch_dist</i>	100
In sphere projection bonus	alpha (α)	3
In sphere straight movement bonus	<i>straight_bonus</i>	10
Bending penalty	eta (η)	0.005, or 0
Plane change penalty	zeta (ζ)	0.005, or 0
Time penalty	<i>time_penalty</i>	0
Length penalty	<i>length_cost</i>	0
Collision penalty	<i>collision_penalty</i>	-50
Success one-off bonus	On reaching <i>target_radius</i>	20000
Early finish bonus	<i>rem/max_steps</i>	Per episode

The needle environment forms the core reward-penalty structure of this code. The needle is rewarded for per-step motion that reduces the Euclidean distance between itself and the target. If the needle reaches a general region (5 mm, in the code as *switch_dist*) around the target, it receives an additional one-off bonus and per-step progress towards the target where the needle projection vector is aligned with the needle to target vector is rewarded and scaled by a constant δ . A second per-step reward is given for straight motion inside *switch_dist*. The success condition is achieved when the needle reaches 2 mm within the target and a large one-off bonus is given, as well as an early termination bonus for finishing an episode scaled by the number of steps remaining (200 – total steps).

The penalty structure is centred on obstacle collisions. A collision terminates the episode with a large negative penalty. Additional penalties η and ζ are applied on steering (to incentivize straight motion unless bending is necessary) and on a change to the bending plane angle to prevent erratic motion. A further *length_cost* and *time_penalty* have been included in the code to force least-distance motions, but experimental tuning indicated that a positive value will largely disincentivize all needle motion and thus these were kept at 0 and require more evaluation before being included in the reward structure. Table 2 above summarizes the values assigned to the reward and penalty variables during training.

The final reward equation for each step is:

$$\begin{aligned}
r_{step} = & \sum_{i=1}^M [\underbrace{w_q(x_{i-1} - x_i)}_{\text{distance reduction reward}} + \mathbf{1}\{x_{i-1} \\
& \leq r_s\} (\underbrace{\delta[(p_i - p_{i-1}) \cdot (t - \widehat{p}_{i-1})]}_{\text{projection bonus in sphere}} + \underbrace{\mathbf{1}\{u=0\} \frac{b_{straight}}{M}}_{\text{straight movement bonus}}) \\
& + \underbrace{\mathbf{1}\{first\ time\ x_i < r_s\} b_{ent}}_{\text{one-off switch_dist entry bonus}} - \underbrace{\eta u}_{\text{bending penalty}} - \underbrace{\zeta |\phi - \phi_{prev}|}_{\text{plane change penalty}} - TP \\
& - \underbrace{50 \mathbf{1}\{collision\}}_{\text{collision penalty}} + \underbrace{\mathbf{1}\{success\} (b_{success} - \lambda L + 100 \frac{\text{remaining steps}}{200})}_{\text{large bonus on success and early termination}}
\end{aligned}$$

M is the number of subpoints in a step, 5 in a straight segment and 15 in a curved segment. Sampling subpoints rather than the entire segment prevents the needle from overshooting the target, allows for an approximate Riemann sum of the projection over the subpoints and is used in visualization for a smooth reconstruction of the curve. x_i and x_{i-1} represent the current and previous distance of the needle to the target for each subpoint. p_i and p_{i-1} are the current and previous needle tip projection vectors. t is the target position vector. ϕ and ϕ_{prev} represent the current and previous bending plane angles. u is the binary steer flag. TP is the time penalty and λL is the total path length penalty.

Over evaluation, given a random seed, we have found that the model generally converges to an obstacle free solution within 500 episodes of training. Environments with obstacles typically require a training length of 2500 episodes. NeedleNav outputs the action vector for each step, and these can be executed in series to reach the target. The experimental setup for the needle stage has been described in the next section.

3.3. Experimental setup

3.3.1 First stage

The key metric to quantify the accuracy of our TDCR is tip position error (TPE). Clinically, the most important performance measure is whether the tip reaches the desired target. We used the Aurora NDI magnetic tracking system to track the endoscope tip in space (figure 14a). The two platforms were placed on a 3D printed bracket to align them and prevent relative movement during testing (figure 14b). The magnetic tip sensor was secured to the endoscope using aluminium tape. To minimise errors due to tendon slack, each motor was rotated to pre-tension the tendons and bring the TDCR to a straight configuration. Initial x, y, z coordinates from the Aurora were noted to reference the tip. There was a mismatch between the reference coordinate systems of the TDCR and the Aurora – the directions of the x and y axes were reversed. Measured x and y values therefore had their signs reversed.

To sample the complete workspace and accuracy of the first stage robot, a grid of 75 points was created, divided into three planes with 25 points each, offset in the z axis. This setup was repeated twice, once for position only FABRIKc control, and once more for combined position and orientation FABRIKc control. To quantify repeatability, the TDCR was commanded to repeat five points eight times. A second test of the positional accuracy was performed by commanding a continuous circle, diamond and triangle trajectory.

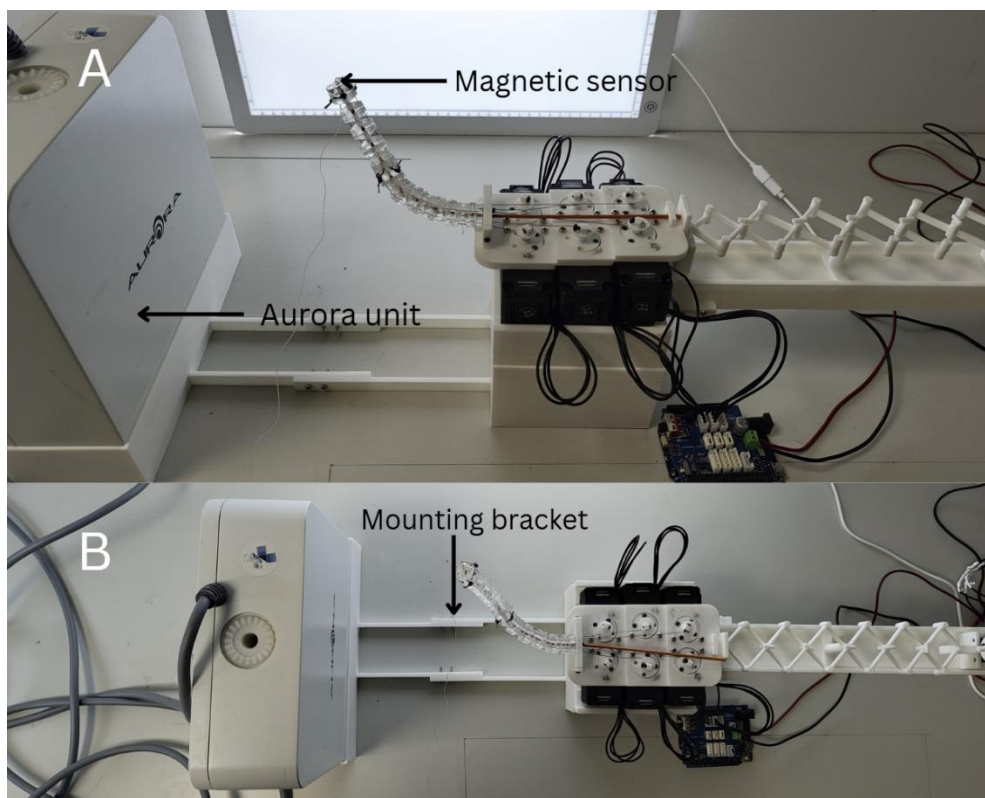


Figure 14: experimental setup of the first stage robot

3.3.2 Second stage

The needle system was tested in a 11.3% w/v gelatine liver phantom (figure 15). kPa stiffness for healthy, fibrotic and cirrhotic tissue have previously been measured through elastography studies.^{40,41} Based on these values, gelatine concentrations of about 7%, 11% and 15% are considered reflective of healthy, fibrotic and cirrhotic tissue. We chose 11.3% as this is a satisfactory compromise (considering this intervention will likely be used in an unhealthy liver) and demonstrates satisfactory bending without tissue damage (the needle would cut through softer phantoms at point of insertion due to buckling). The dimensions of the phantom were 18 cm x 13 cm x 5 cm, matching the rough size of a normal adult liver.

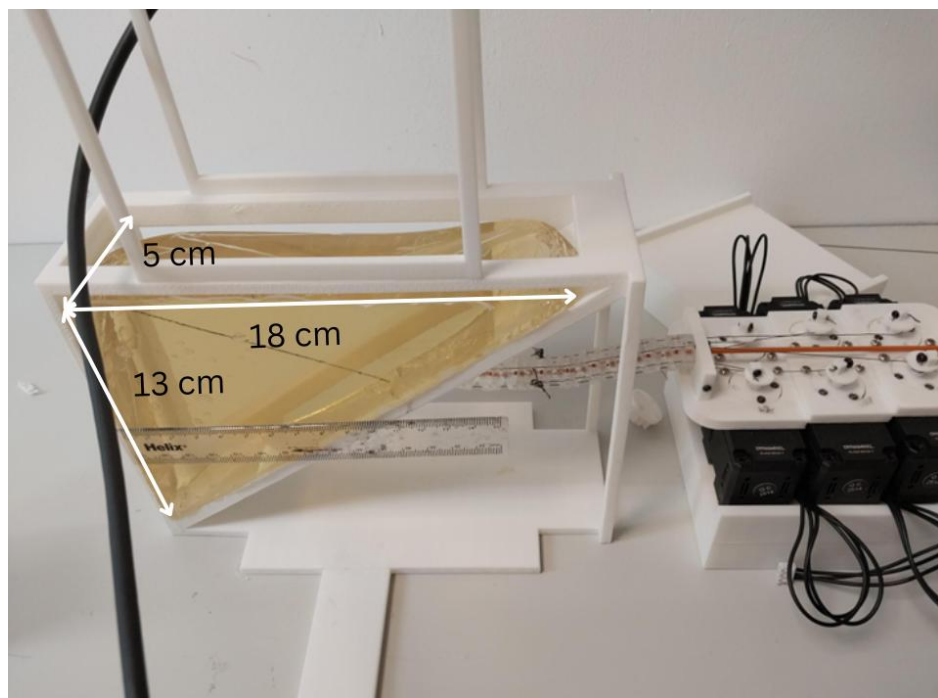


Figure 15: needle in gelatine liver phantom, upward angled configuration

The needle was tracked using a proprietary camera-based software.⁴² Two Logitech BIRO stereo cameras were placed to the side of and above the phantom (figure 16a). Using thresholding, the solid needle body was identified, referenced and highlighted for tracking (figure 16b, c). Points were sampled at 0.5 Hz.

Eight entry point-entry orientation-target point triplets were selected for sampling. Four straight, three upward angled and two laterally angled entry orientations used as the TDCR may be in various configurations during actual endoscopy. NeedleNav was first used to generate obstacle free trajectories. Based on visualisation, an obstacle mimicking a blood vessel was placed directly in the path, resulting in a failed trajectory. SAC actor and critic weights for the obstacle free trajectory were then saved and removed and the model was retrained to generate an obstacle avoidance trajectory (figure 17). Obstacle free trajectories were sampled once while obstacle avoidance trajectories were sampled thrice.

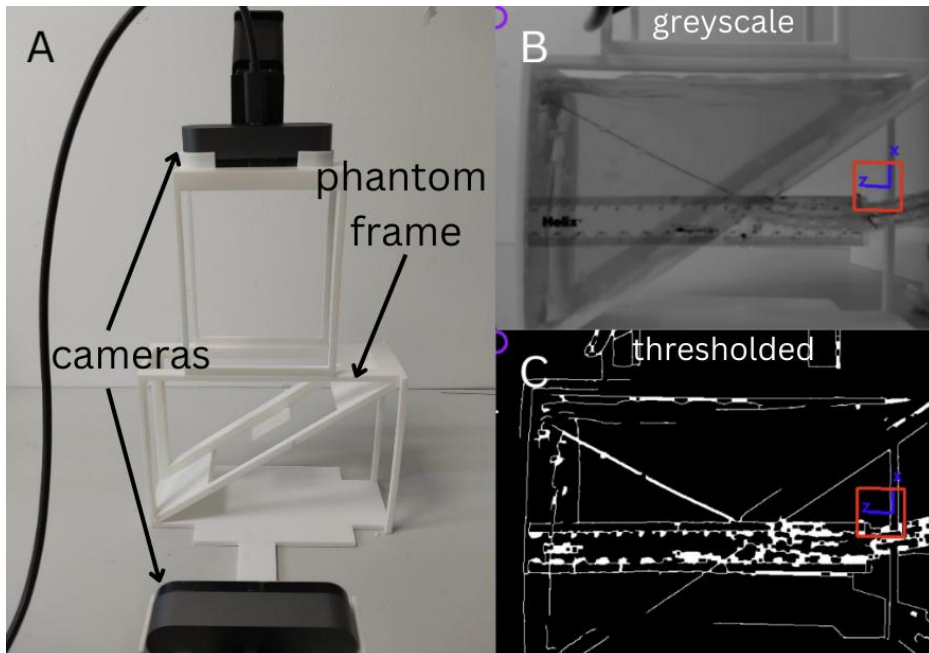


Figure 16: a) experimental setup for the steerable needle, b) grayscale tracking of the needle, c) thresholded tracking of needle

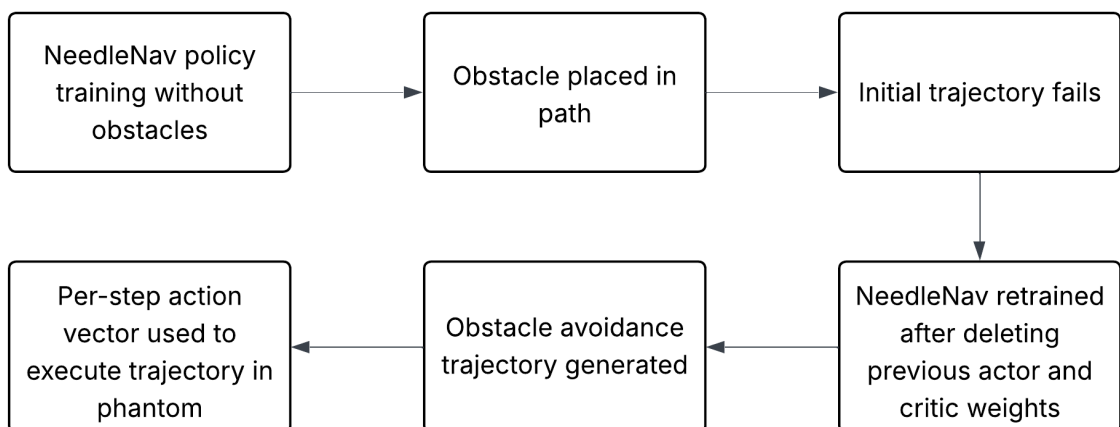


Figure 17: NeedleNav experimental workflow

4. Results

4.1. First stage evaluation

4.1.1. Point-to-point accuracy

Table 3: TDCR accuracy metrics

Test (mm)	Euclidean (mm)	MAE	Euclidean (mm)	RMSE	SD (mm)
PC control	20.86		22.17		7.58
POC Commanded vs FABRIKc	17.25		21.3		12.48
POC control	20.44		21.84		7.8

Figure 16 displays the results of our 75-point positional accuracy tests. Each point varied in the x and y axis by 30 mm, defining a square plane of side 120 mm. For position only control (PC) planes were sampled in z axis values of 50, 65 and 80 mm. For position and orientation control (POC), planes were sampled in slices of 50, 70 and 90 mm. In the case of PC, FABRIKc positions are equal to commanded positions. Euclidean mean absolute error (MAE), root mean square error (RMSE) and standard deviation (SD) for all positional tests are in table 3 above.

As discussed previously, the TDCR is underactuated for a POC task. FABRIKc outputs the closest possible position value while adhering to the orientation command. This introduces an error between the commanded point and the FABRIKc point (figure 17b).

Observing the POC FABRIKc points gives us useful insights into the workspace of the robot. Some commanded points sampled at $z = 70$ and $z = 90$ were outside the workspace of the robot, and thus FABRIKc output the closest achievable position value. This resulted in the formation of a dome-like structure. This closely matches the predicted workspace as shown in figure 18.

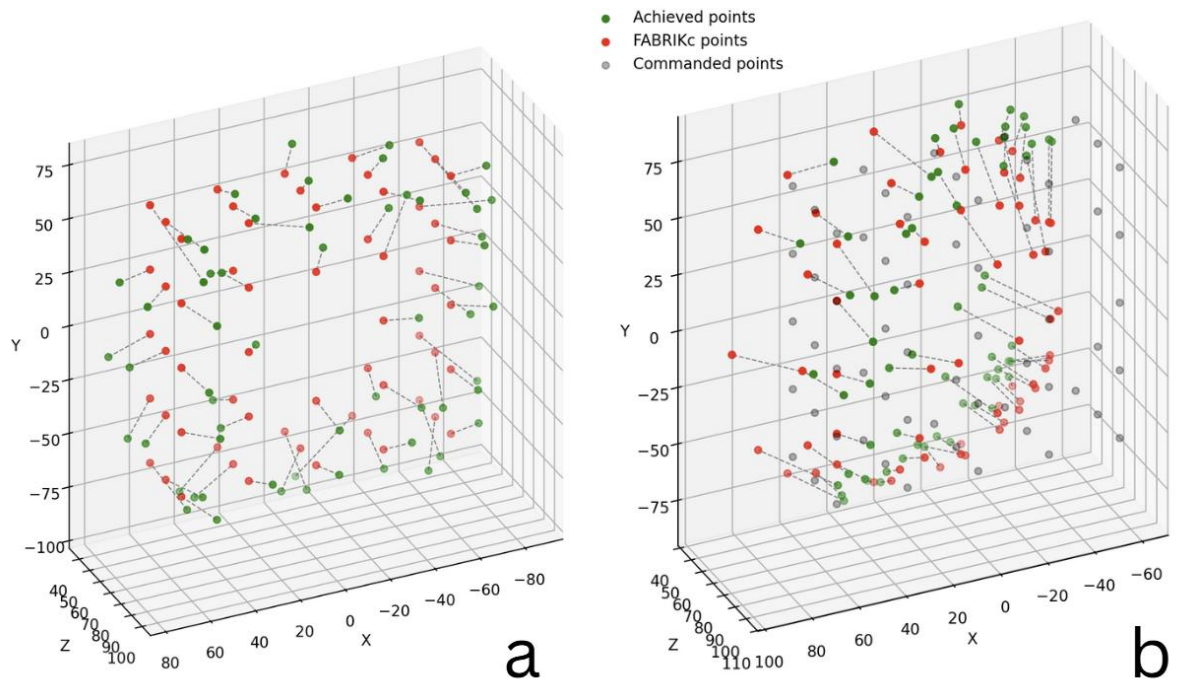


Figure 17: Point-to-point accuracy testing. a) FABRIKc position only, b) FABRIKc position and orientation.

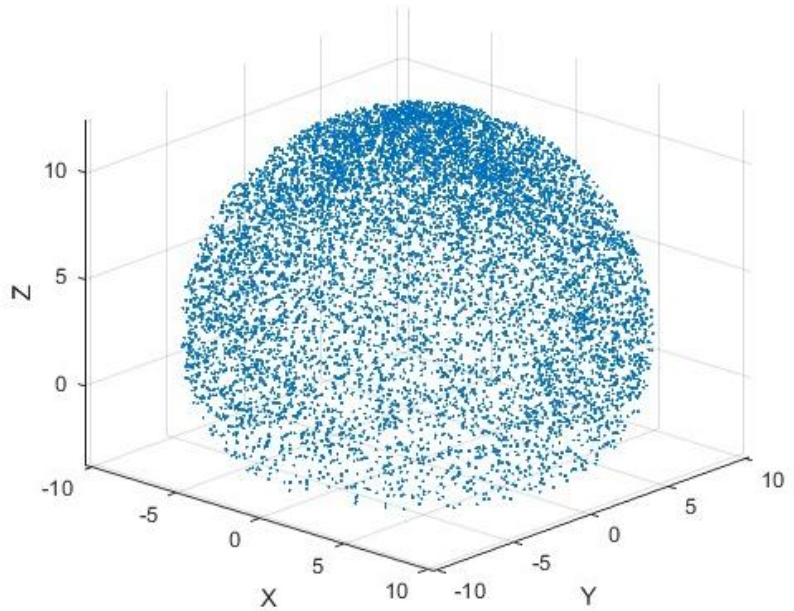


Figure 18: Modelled workspace of the TDCR

To better visualise the error, surface heatmaps of the achieved points and FABRIKc points were created using bivariate cubic interpolation from the gridata function in MATLAB. Figure 19 displays the heatmap for PC FABRIKc. Yellow regions indicate higher 3D error. The general trend appears to be higher 3D error at the outlines and lower error towards the centre of the plane (discussed in section 4.1.4).

Figure 20 displays the surface heatmaps for POC FABRIKc between the FABRIKc points and robot achieved points. The achieved points form an asymmetric dome with a sloping side, also apparent in figure 17b. This indicates that the robot is biased to the right side, likely due to mechanical asymmetry discussed in detail in section 4.1.4 below.

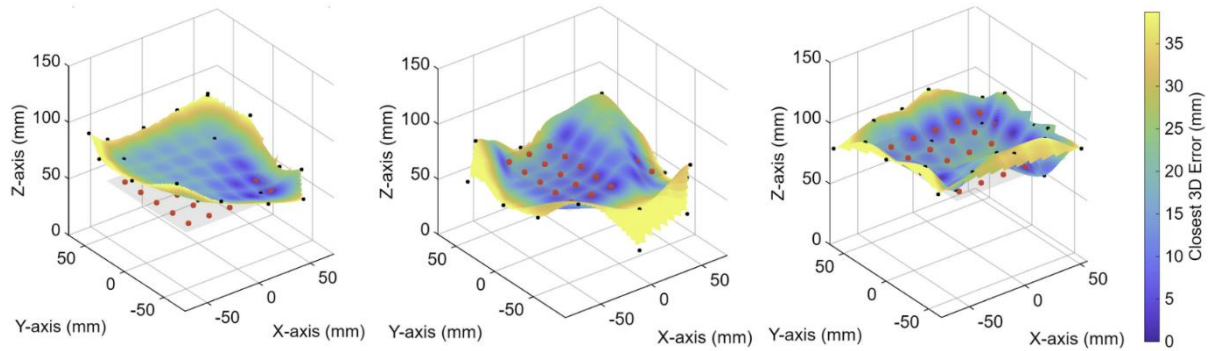


Figure 19: Error heatmap for PC FABRIKc

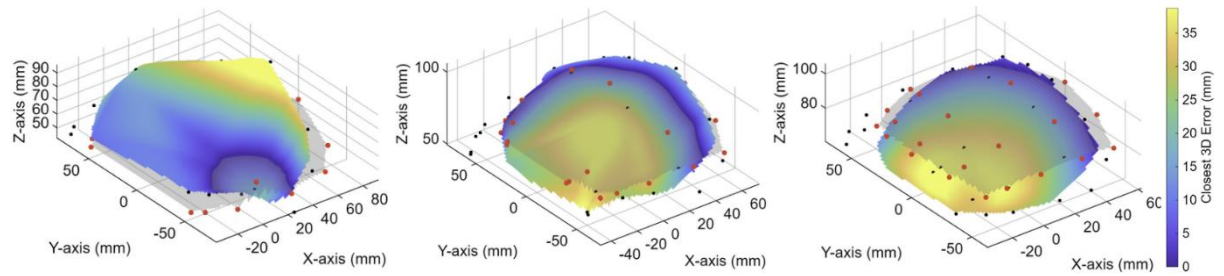


Figure 20: Error heatmaps of POC FABRIKc

4.1.2. Shape generation accuracy

Table 4: TDCR trajectory accuracy metrics

Test (mm)	Euclidean MAE (mm)	Euclidean RMSE (mm)	SD (mm)
Circle trajectory	15.12	15.80	4.6
Diamond trajectory	22.98	23.96	6.78
Triangle trajectory	27.24	29.09	10.20

The robot was commanded to execute three trajectories once. A circle trajectory ($r = 60 \text{ mm}$) was chosen to demonstrate accuracy for a smooth, continuous task (figure 21). Increments between each point were small, allowing a precise assessment of the TDCR's curved path following deviation.

The second and third trajectories were a diamond and an isosceles triangle ($s = 60 \text{ mm}$) (figure 22, figure 23). These shapes were used to evaluate performance on sharp corners, which usually involves more significant changes to configuration per increment.

Execution of these trajectories has direct clinical relevance. The diameter of an adult empty stomach varies between 5 cm and 15 cm , which will expand during endoscopy through insufflation. The circle trajectory demonstrates that at the centroid of the stomach, the TDCR can operate within the full diameter of the working cavity. Results of trajectory following have been analysed in section 4.1.4.

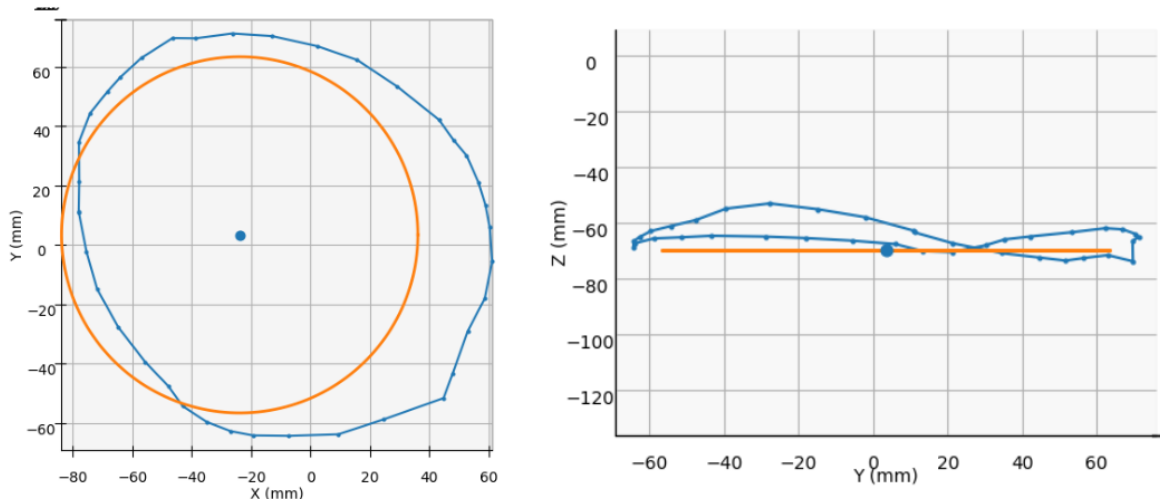


Figure 21: Circle trajectory view in the XY and ZY axes. Orange is reference circle, blue is real trajectory

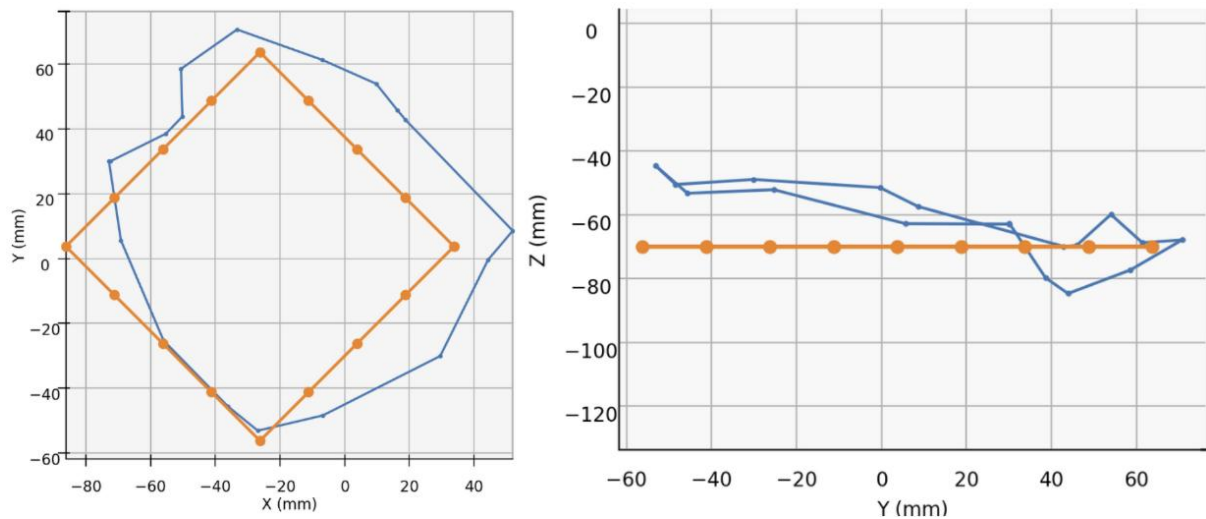


Figure 22: Diamond trajectory view in the XY and ZY axes

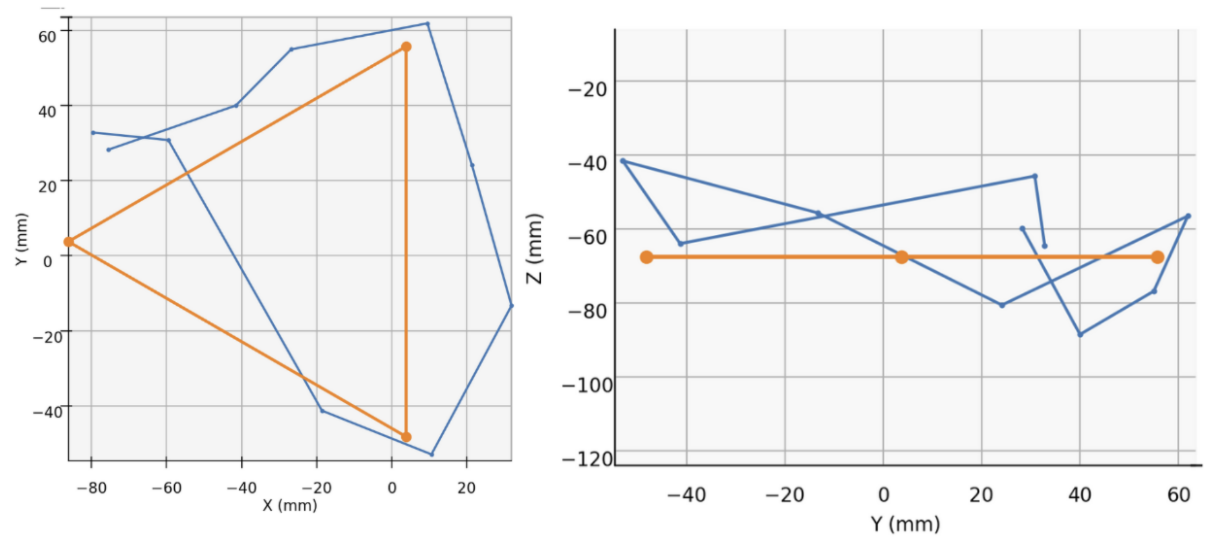


Figure 23: Triangle trajectory in the XY and ZY axes

4.1.3. Repeatability

Table 5: Repeatability testing

Index (ref. figure 24)	Commanded point (POS control) (mm)	Point from FABRIKc (mm)	Mean achieved (mm)	SD (mm)	Repeatability (3*SD) (mm)
a	(50, 40, 70)	(54.1, 50.5, 79.1)	(46.7, 34.5, 96.6)	0.92	2.76
b	(40, 60, 70)	(40.2, 64.1, 72.2)	30.7, 50.8, 90.7	0.39	1.18
c	(40, 40, 90)	(40.1, 41.3, 91.9)	(37.5, 30.7, 94.6)	0.84	2.53
d	(60, 60, 60)	(60.9, 62.0, 60.7)	(56.9, 63.6, 87.4)	0.45	1.34
	Average	-	-	0.65	1.95

To assess the repeatability of the robot, four points were sampled, each repeated eight times. Table 3 above displays the key metrics to measure repeatability from each point. Figure 24 visualises the achieved points in relation to their mean.

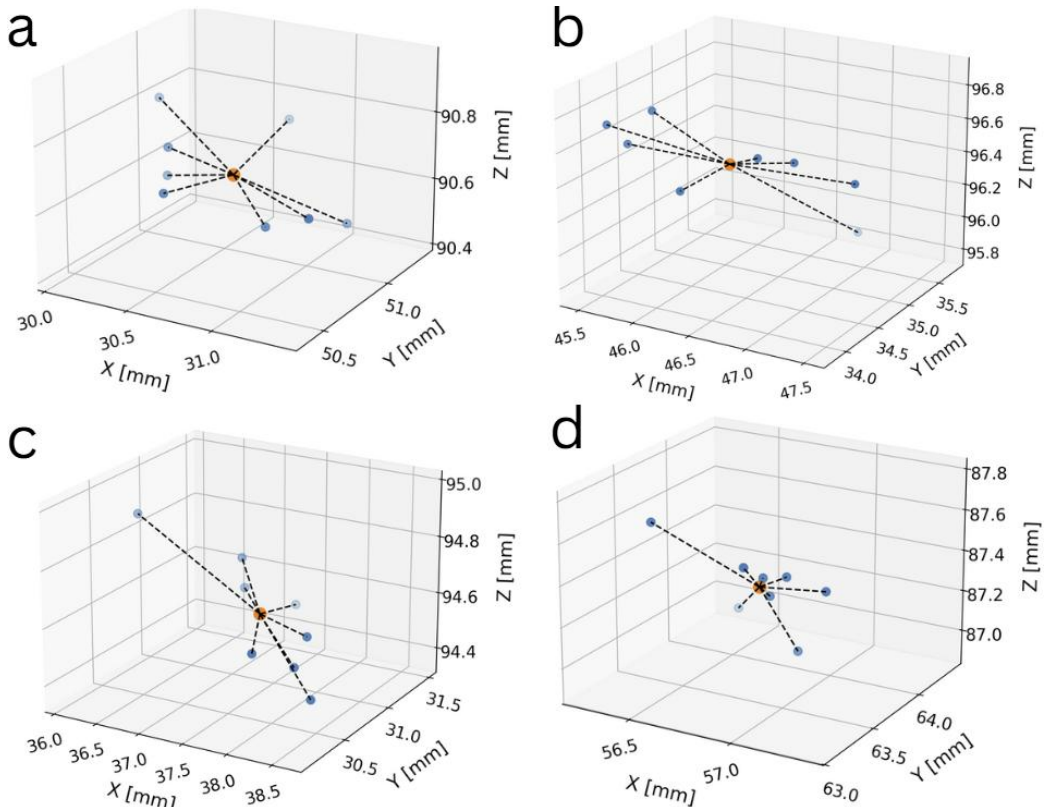


Figure 24: Visualisation of the mean (orange) and achieved points (blue) connected by straight lines.

4.1.4. Analysis

Across tests, the TDCR is generally able to reach a point with a 20 mm 3D error. This is outside the acceptable range for GI endoscopic applications, which would typically require a tip position error $< 2 \text{ mm}$. In fact, this proposed application to FNA might require an even smaller error, as the positional accuracy of the needle is dependent on the accuracy of the TDCR. The error is likely due to a combination of:

- a) **Unequal tendon tension:** before testing, the robot was set to a straight zero-configuration, and all tendons were pre-tensioned so that pulley rotation should produce an immediate deflection rather than tightening slack. Tendon tension was measured by manually pulling on them – this is an inaccurate approach and will contribute to backlash.
- b) **Tendon-disc friction:** while the needle guide has steel bushings to reduce friction, the spacer discs in the TDCR do not. The friction produced by tendon-disc interaction will lead to hysteresis. Furthermore, the steel wire-rope tendons, are prone to fraying under sliding contact, which changes their effective diameter, roughness and compliance.
- c) **Distal tendon lengths change on proximal segment bending:** tendons actuating the distal segment pass through the proximal segment. On bending the proximal segment, the effective distal tendon lengths change. This is not accounted for in our length calculation function *casecompute1*. It partially explains the higher error at margins observed in PC FABRIKc control: points on the margins require a larger proximal segment bending compared to the distal segment (figure 25a). This will scale the overall tip inaccuracy. This is as opposed to points closer to the centre, which require little proximal segment curvature and larger distal bending (figure 25b).
- d) **Constant curvature assumption:** FABRIKc assumes piecewise constant curvature. Although this is a close approximation, segments exhibit non-uniform curvature, which will lead to error.

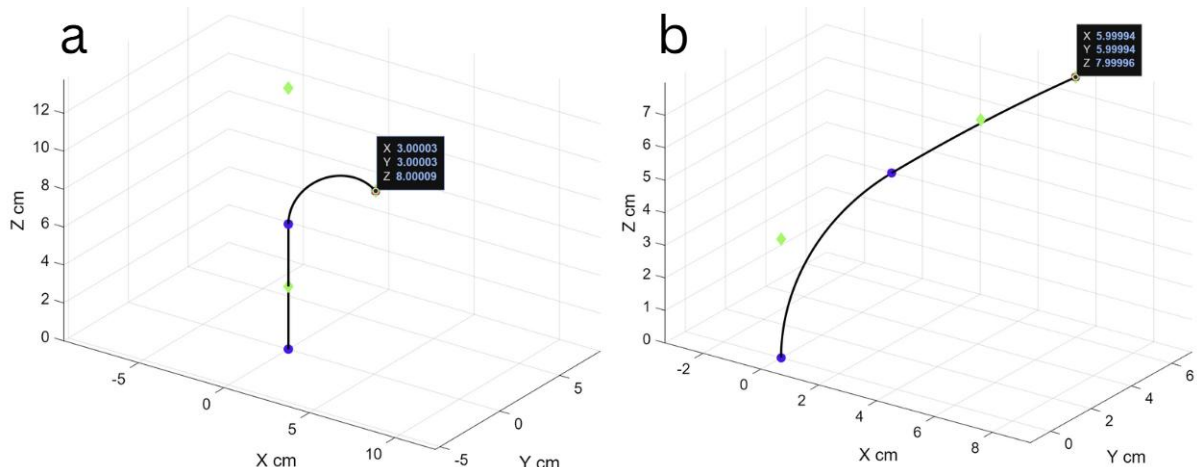


Figure 25: a) FABRIKc visualisation for target (3, 3, 8), b) target (6, 6, 8)

- e) **Registration errors:** Although the NDI and robot were secured with a bracket, the magnetic sensor fixed to the tip was prone to minor displacement during robot motion.

Analysing the trajectory errors, the circle has the lowest MAE and RMSE across tests. This is expected – PC and POC FABRIKc control sample a much larger workspace with larger movement increments between points. The circle requires small incremental motion for points that are relatively easily reachable. The higher error for the diamond and triangle validate the expectation that sharper edges are more difficult to execute compared to smoother curves.

A repeatability of 1.95 mm is promising, although the expected range for clinical applications would be submillimetre scale. It indicates that the MAE is from a systematic bias that applies to all points, rather than random variability in the motors, TDCR or control software.

4.2. Second stage evaluation

4.2.1. Results

Testing of NeedleNav and the steerable needle platform was performed by sampling eight trajectories as described in section 3.3.2, selected using the following criteria:

- (a) effectively demonstrates curvature of the needle
- b) reflects intended clinical use i.e. deep-seated lesions in the right lobe
- c) the x axis length is long enough for the needle to curve enough and avoid obstacles
- d) showcases various insertion orientations

Figure 26 shows a relatively simple trajectory that only bends in the XY plane. The relative position of the target from the entry point was $(12, -2, 0)\text{ cm}$ with a straight entry orientation.

Figure 26a displays the XY view of NeedleNav trajectories. As is expected, the red obstacle free trajectory has an initial curvature which aligns the needle and the target, and then simple straight motion. However, as the vessel obstacle is placed in its path, the trajectory fails. The blue obstacle avoidance trajectory continues straight motion until it clears the obstacles and then begins bending. This is reflected in the real trajectories (figure 26b, d) – while the obstacle free trajectory has assumed a diagonal path to the target from the beginning, the obstacle avoidance trajectory has delayed bending, curved and then proceeded straight to target. Needle tracking was affected by noise from folds on the gelatine phantom appearing on the thresholding interface, which limited the accuracy of trajectory reconstruction. However, we can confirm that the true needle trajectory was generally consistent with the NeedleNav trajectory through visual inspection of figure 24e and 24f.

For this first trajectory, the relative tip position for the obstacle free trajectory was: $(105.3, -16.54, 2.4)\text{ mm}$. The tip position error was $(14.7, 3.46, 2.42)\text{ mm}$. The relative tip position for the obstacle avoidance trajectory was: $(107.4, 12.52, 1.9)\text{ mm}$. The tip position error was $(12.6, 7.48, 1.9)\text{ mm}$.

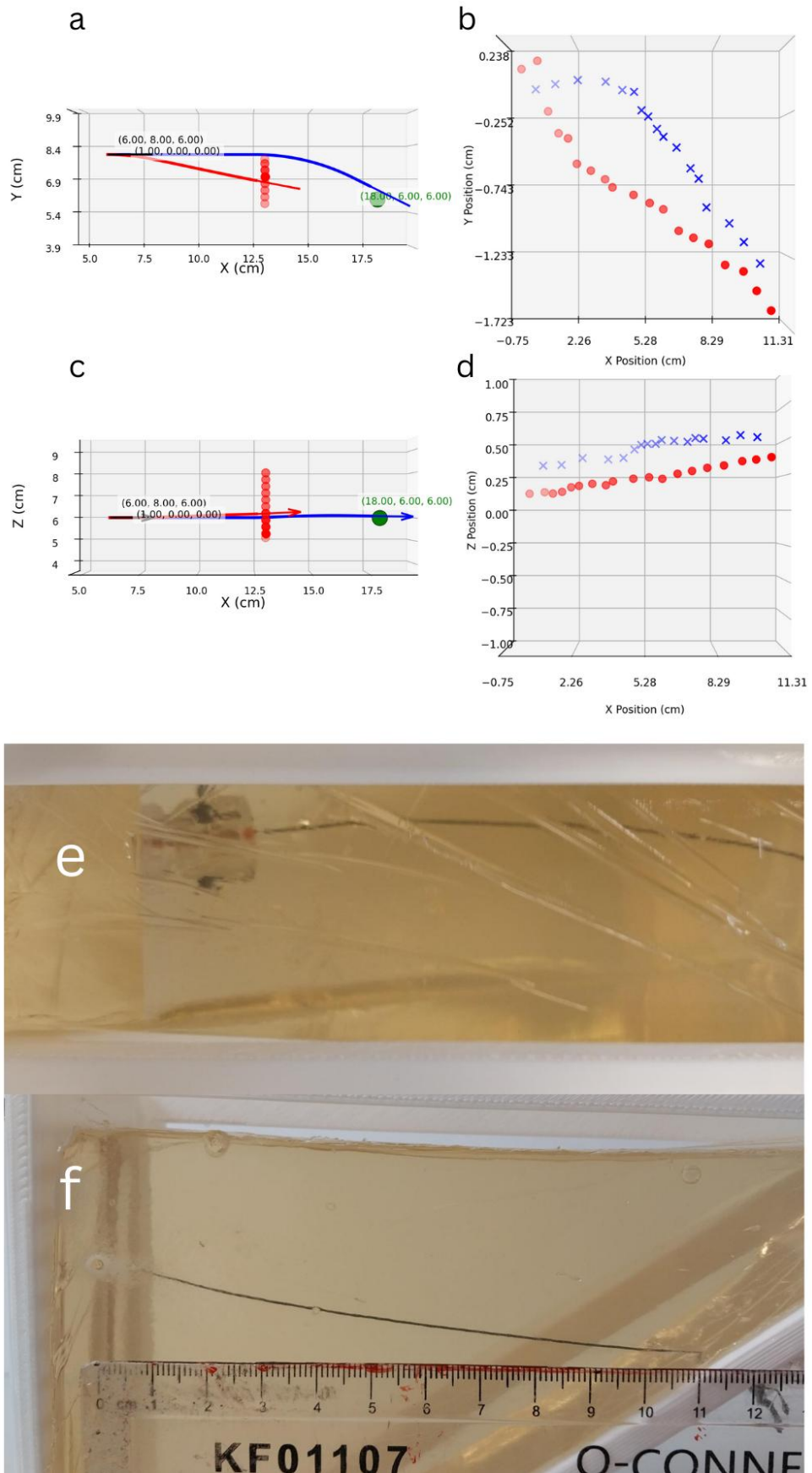


Figure 26: XY view of the SAC obstacle free and obstacle avoidance trajectories, b) XY view of real trajectories achieved by the needle, c) XZ view of the SAC trajectories, d) XZ view of the real trajectories, e) XY view in-phantom, f) mirrored XZ view in-phantom. Insertion orientation was [1, 0, 0].

For the second target $(120, 30, -30) \text{ mm}$, the relative tip position for the obstacle free trajectory was: $(121.87, 14.12, -13.14) \text{ mm}$. The tip position error was $(1.87, -15.88, 16.86) \text{ mm}$. The relative tip position for the obstacle avoidance trajectory was: $(115.38, 10.72, -12.16) \text{ mm}$. The tip position error was $(4.62, 19.28, 17.84) \text{ mm}$.

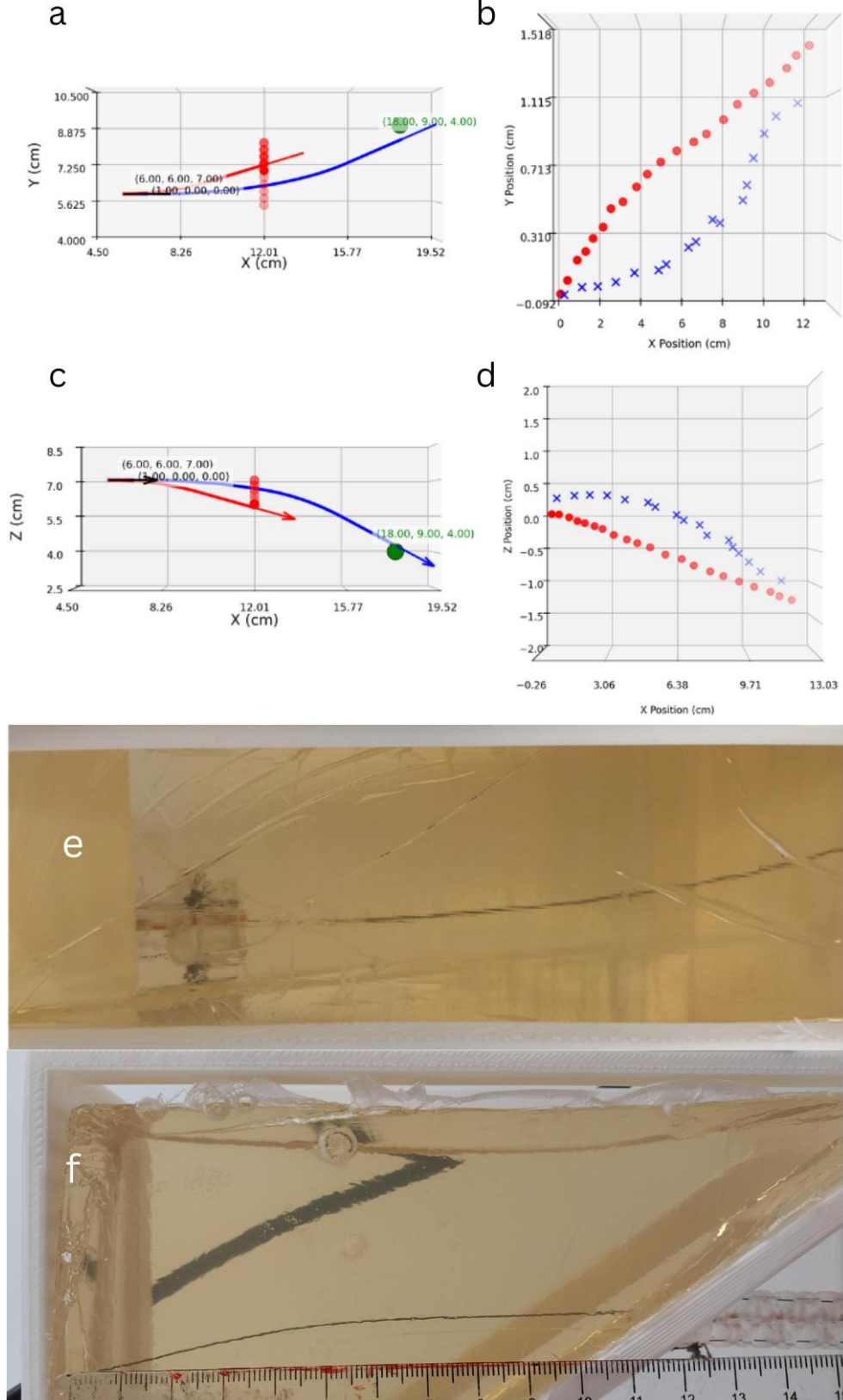


Figure 27: XY view of the SAC obstacle free and obstacle avoidance trajectories, b) XY view of real trajectories achieved by the needle, c) XZ view of the SAC trajectories, d) XZ view of the real trajectories, e) XY view in-phantom, f) mirrored XZ view in-phantom. Insertion orientation was $[1, 0, 0]$.

For the third target ($120, 30, -30$) mm, the relative tip position for the obstacle free trajectory was: ($106.92, 11.02, -13.50$) mm. The tip position error was ($13.08, 18.98, 16.5$) mm. The relative tip position for the obstacle avoidance trajectory was: ($110.31, 19.31, -17.859$) mm. The tip position error was ($9.69, 10.69, 12.14$) mm.

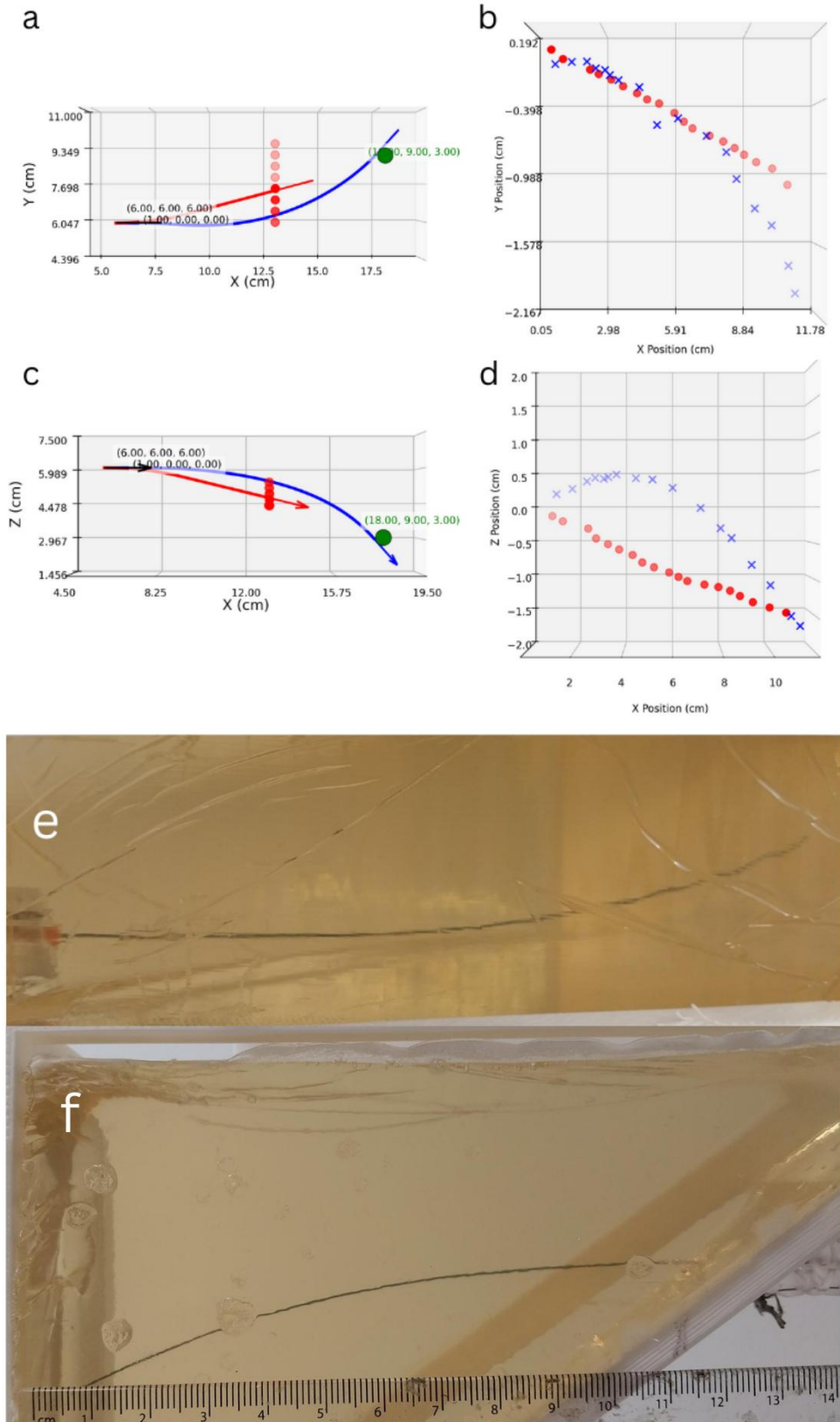


Figure 28: XY view of the SAC obstacle free and obstacle avoidance trajectories, b) XY view of real trajectories achieved by the needle, c) XZ view of the SAC trajectories, d) XZ view of the real trajectories, e) XY view in-phantom, f) mirrored XZ view in-phantom. Insertion orientation was [1, 0, 0].

For the fourth target ($115, 10, -40$) mm, the relative tip position for the obstacle free trajectory was: ($102.65, 8.36, -21.94$) mm. The tip position error was ($12.35, 1.64, 18.06$) mm. The relative tip position for the obstacle avoidance trajectory was: ($101.21, 8.10, -13.40$) mm. The tip position error was ($13.79, 1.9, 26.6$) mm.

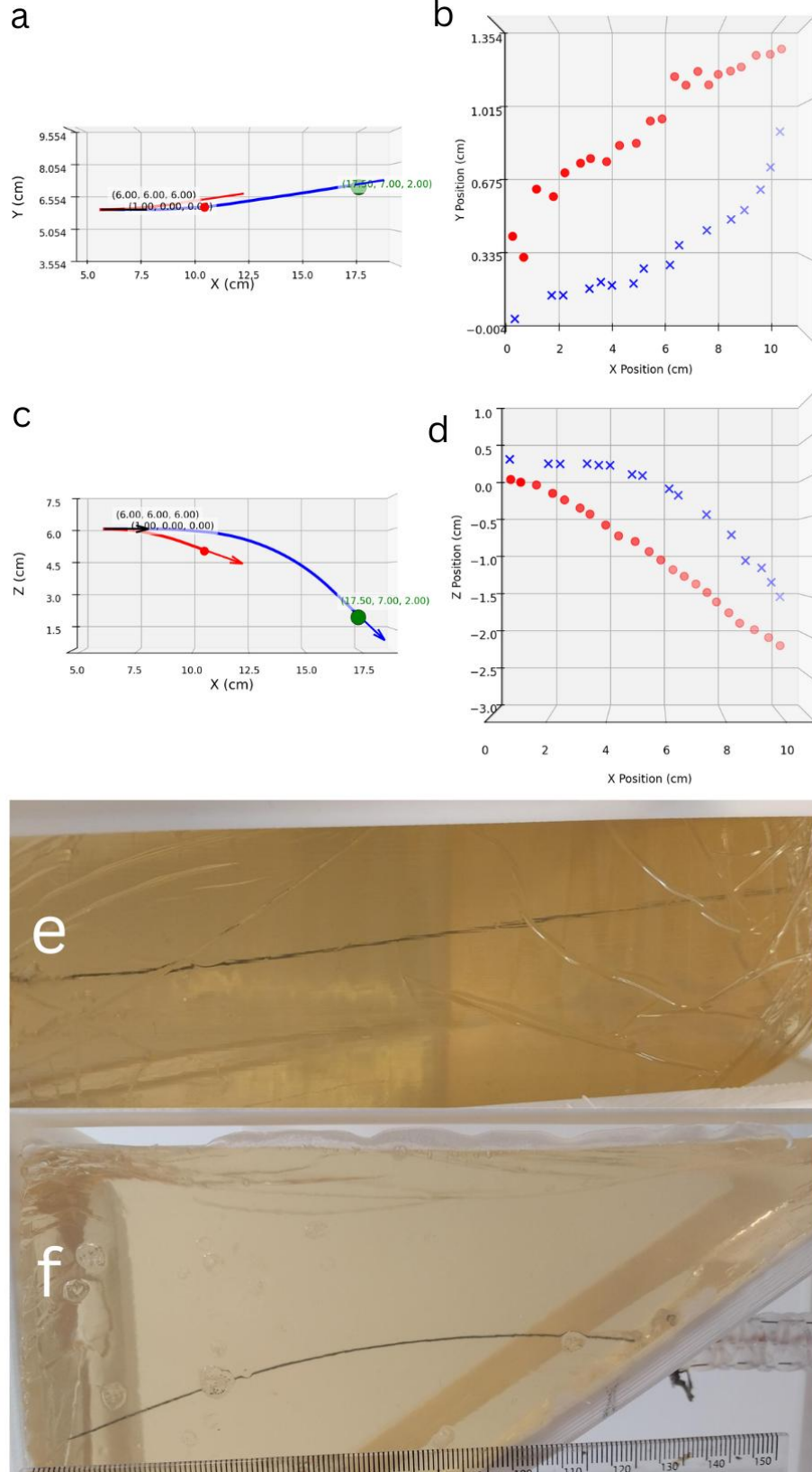


Figure 29: XY view of the SAC obstacle free and obstacle avoidance trajectories, b) XY view of real trajectories achieved by the needle, c) XZ view of the SAC trajectories, d) XZ view of the real trajectories, e) XY view in-phantom, f) mirrored XZ view in-phantom. Insertion orientation was [1, 0, 0].

For the fifth target (95, 30, 53) mm, the relative tip position for the obstacle free trajectory was: (92.34, 21.78, 49.60) mm. The tip position error was (2.66, 8.22, 3.40) mm. The relative tip position for the obstacle avoidance trajectory was: (96.32, 17.01, 46.80) mm. The tip position error was (1.32, 12.99, 6.20) mm.

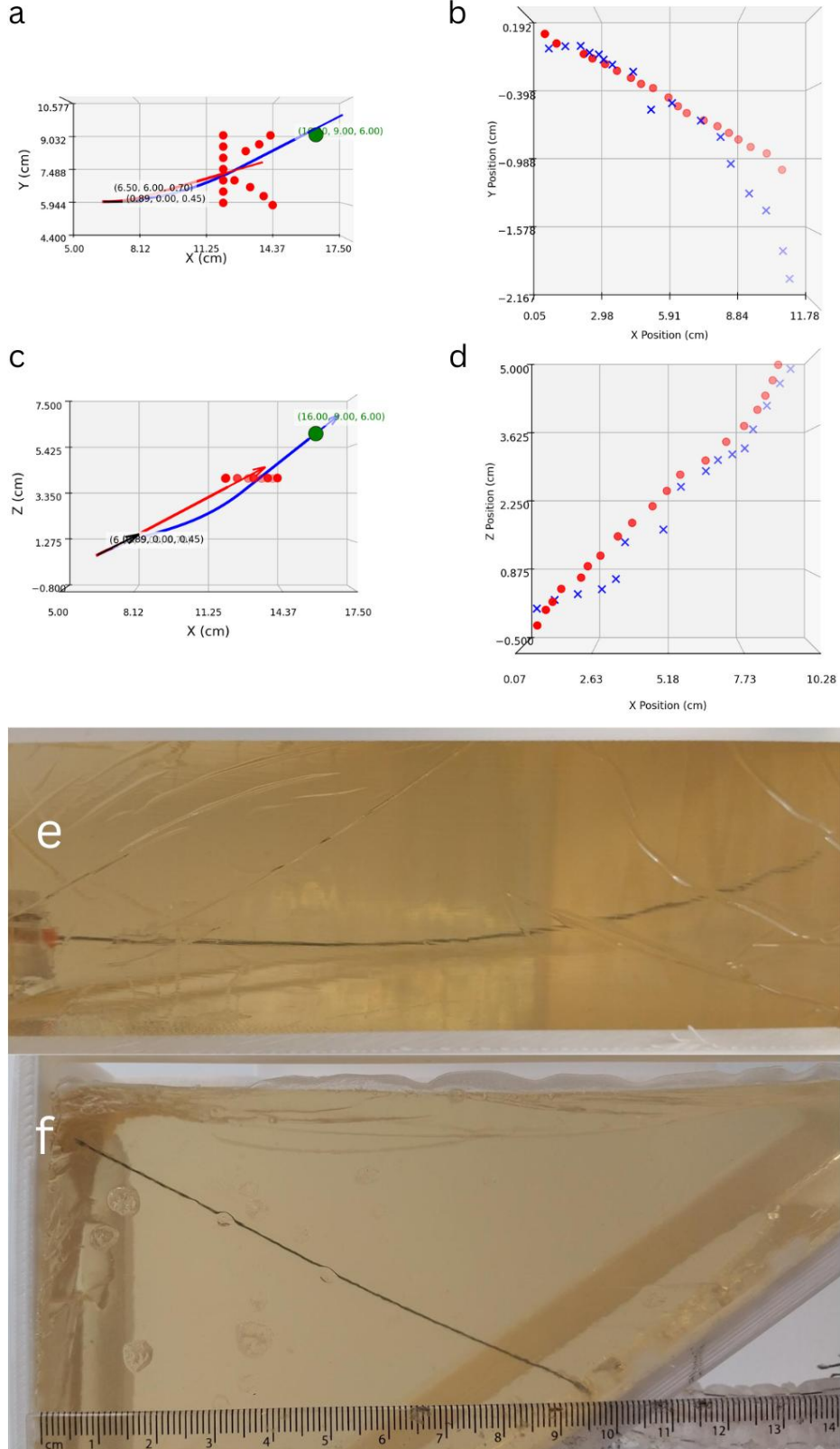


Figure 30: XY view of the SAC obstacle free and obstacle avoidance trajectories, b) XY view of real trajectories achieved by the needle, c) XZ view of the SAC trajectories, d) XZ view of the real trajectories, e) XY view in-phantom, f) mirrored XZ view in-phantom. Insertion orientation was [0.89, 0, 0.45].

For the sixth target (110, 30, 60) mm, the relative tip position for the obstacle free trajectory was: (105.32, 12.23, 58.439) mm. The tip position error was (4.68, 17.77, 1.65) mm. The relative tip position for the obstacle avoidance trajectory was: (103.33, 3.40, 56.39) mm. The tip position error was (6.67, 26.6, 3.61) mm.

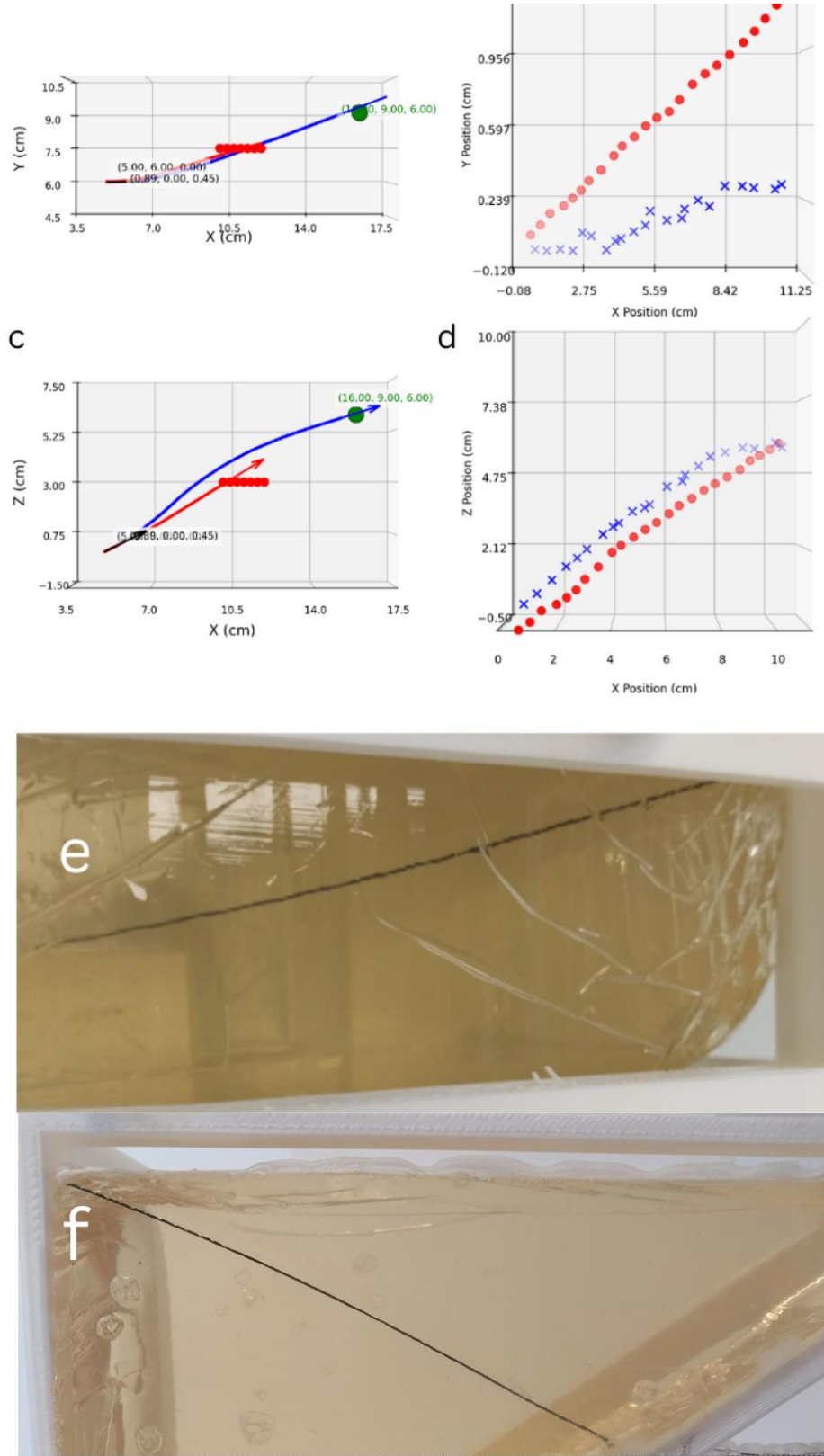


Figure 31: XY view of the SAC obstacle free and obstacle avoidance trajectories, b) XY view of real trajectories achieved by the needle, c) XZ view of the SAC trajectories, d) XZ view of the real trajectories, e) XY view in-phantom, f) mirrored XZ view in-phantom. Insertion orientation was [0.89, 0, 0.45].

For the seventh target ($120, 20, -20$) mm, the relative tip position for the obstacle free trajectory was: ($112.87, 14.21, -8.15$) mm. The tip position error was ($7.13, 5.79, 11.85$) mm. The relative tip position for the obstacle avoidance trajectory was: ($113.72, 14.67, -9.72$) mm. The tip position error was ($6.28, 5.33, 10.28$) mm.

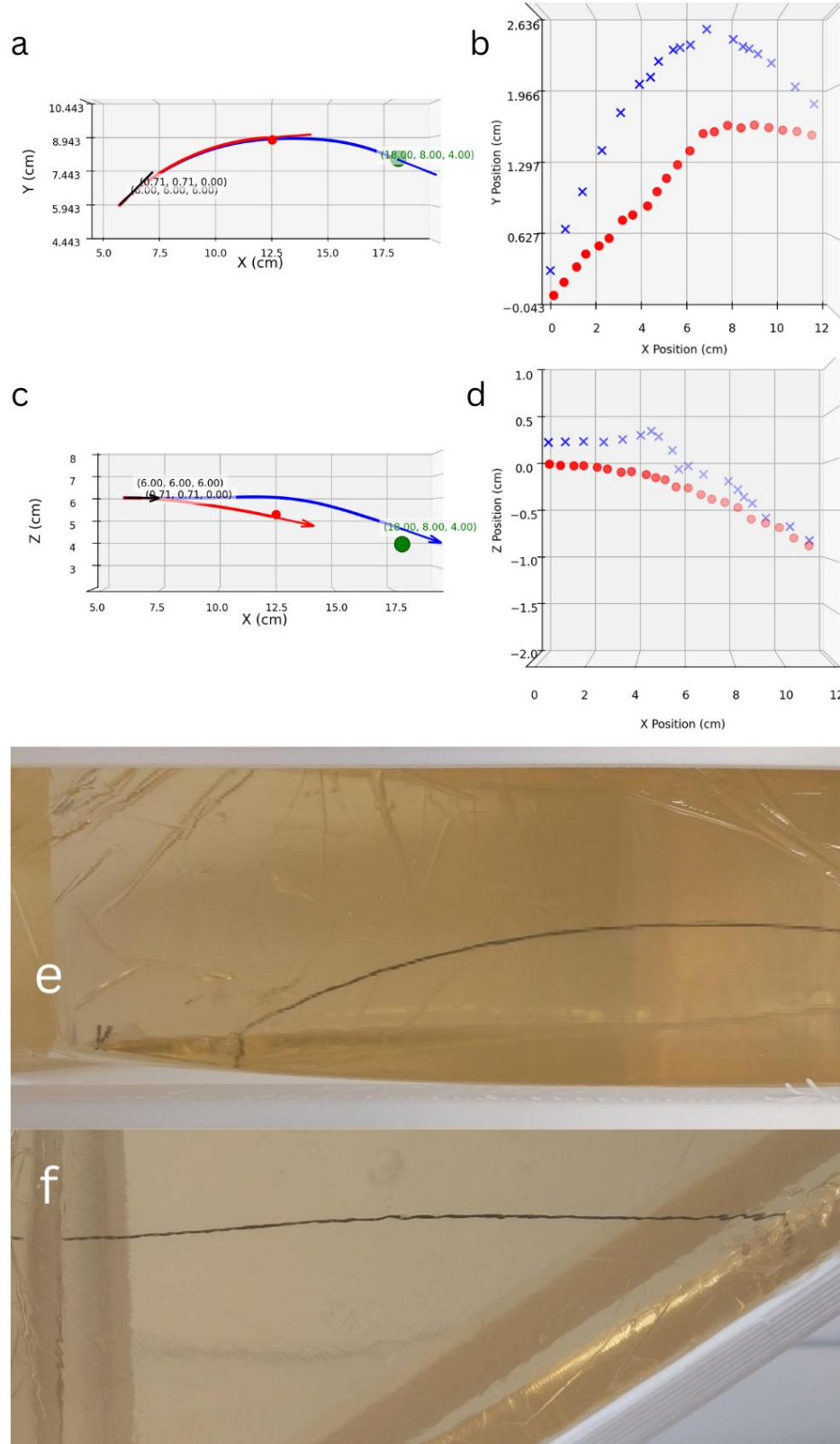


Figure 32: XY view of the SAC obstacle free and obstacle avoidance trajectories, b) XY view of real trajectories achieved by the needle, c) XZ view of the SAC trajectories, d) XZ view of the real trajectories, e) XY view in-phantom, f) mirrored XZ view in-phantom. Insertion orientation was [0.71, 0.71, 0].

For the eighth target $(120, -20, -20) \text{ mm}$, the relative tip position for the obstacle free trajectory was: $(114.59, -15.04, -12.21) \text{ mm}$. The tip position error was $(5.41, 4.96, 7.79) \text{ mm}$. The relative tip position for the obstacle avoidance trajectory was: $(121.66, -16.74, -12.34) \text{ mm}$. The tip position error was $(1.66, 3.26, 7.66) \text{ mm}$.

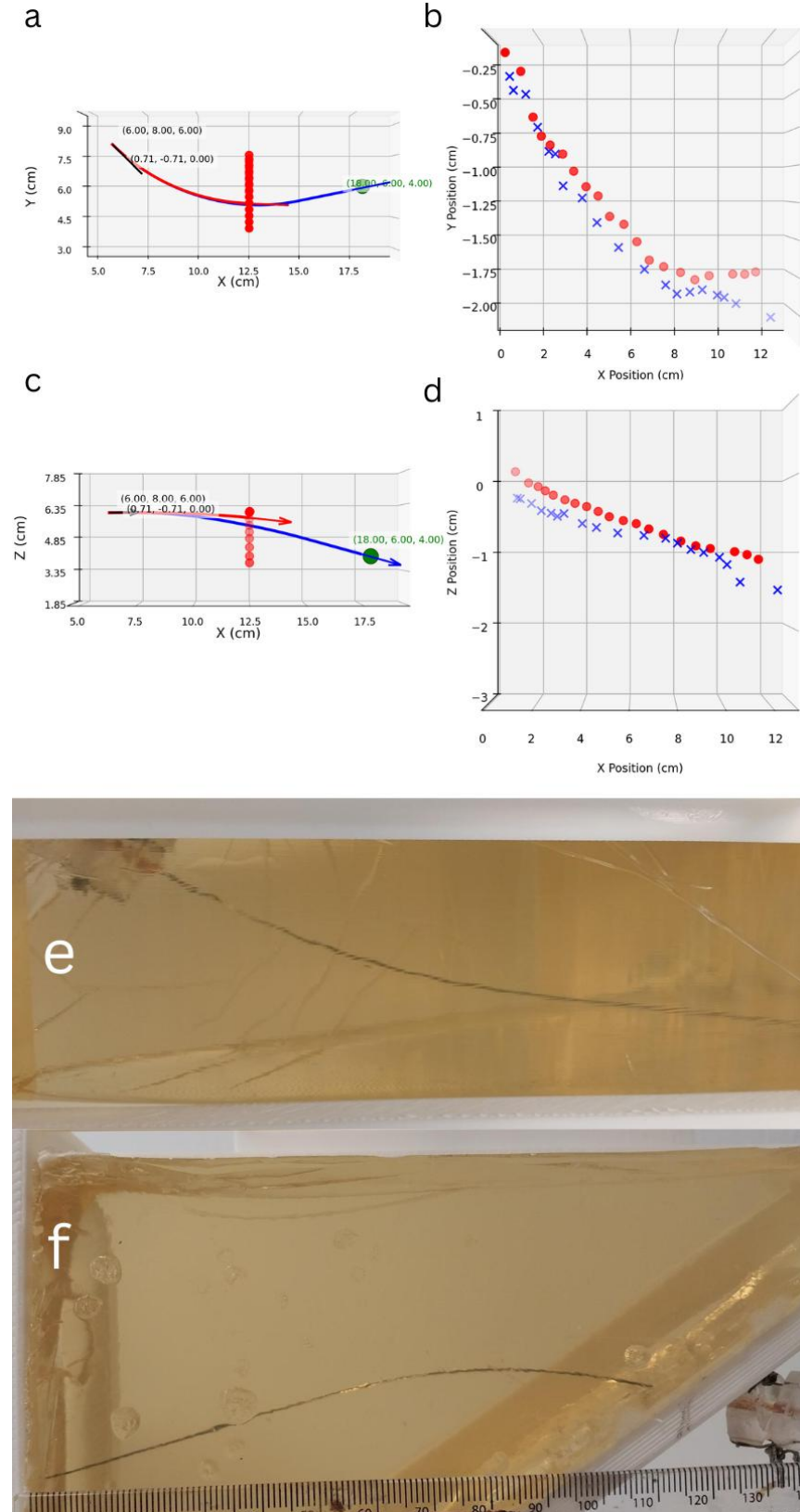


Figure 33: XY view of the SAC obstacle free and obstacle avoidance trajectories, b) XY view of real trajectories achieved by the needle, c) XZ view of the SAC trajectories, d) XZ view of the real trajectories, e) XY view in-phantom, f) mirrored XZ view in-phantom. Insertion orientation was $[0.71, -0.71, 0]$.

4.2.2. Analysis

Table 6: Average error for obstacle free and obstacle avoidance trajectories

Test (mm)	Euclidean MAE (mm)	Euclidean RMSE (mm)	SD (mm)	Percentage error
Obstacle free trajectories	17.78	18.79	6.08	14.42%
Obstacle avoidance trajectories	21.78	23.47	8.75	17.66%

The trajectories executed validate the principle of two DoF control through rotation and translation. When comparing the obstacle free and obstacle avoidance trajectories, the observed deflection in needle path broadly aligns with the predicted path created by NeedleNav. However, positional error limits reliable assessment of true obstacle avoidance (to be able to differentiate whether the true trajectory hit the obstacle because of an incorrect commanded path, or the inherent tip accuracy). Clinical translation would require submillimetre scale error and a considerably tighter curvature to avoid a complex network of obstacles. The average errors achieved by our system are in table 6 above.

Inaccurate curvature is likely to be the major cause for the error; as stated in section 3.2.1, curvature is not uniform over the entire needle. During initial tests to measure the curvature, we observed that the curvature could vary from 33 m^{-1} (for insertion of the distal notched section only) to 6 m^{-1} (for a longer insertion length). After repeated testing, an estimate on the lower end of the scale was chosen (10.44 m^{-1}) as most reflective of the true curvature, but this is an approximation and thus the key reason for our observed error.

Other factors include:

- a) **Inaccurate motor resolution:** the XL-330 servos demonstrated a practical resolution of 1 mm per 100 encoder increments in phantom. This value is likely to have changed as the force required for forward translation increased with insertion depth and needle curvature.
- b) **Variation in phantom stiffness and integrity:** the gelatine phantom was prone to ‘shrinking’ and hardening over time. For this reason, new phantoms were used after 8 hours of continuous testing. However, some alteration in stiffness over that period is likely, altering curvature and per step insertion length. Additionally, continuous insertion-withdrawal for each trajectory may have created areas in the phantom with reduced stiffness.
- c) **Insertion angle inaccuracy:** the TDCR was first commanded to reach the required orientation. The angle was then checked and manually refined using a protractor as reference. This method is inaccurate and underlines the importance of a TDCR that has low position and orientation error.

- d) **Tip lag during rotation (snapping):** in the case of non-straight TDCR orientations, it was observed that when the needle was almost retracted, rotation from the base did not result in a corresponding rotation at the tip. Instead, the needle would jump between angles in large increments. This is most likely due to friction between the notches and the internal spring backbone, as the needle was able to freely rotate once this section was extended. To address this, TDCR configurations with high curvature were avoided and the needle tip and distal central backbone were lubricated with WD-40. However, some residual lag is likely to have contributed to error, particularly in the initial steps of each trajectory.
- e) **Needle buckling** in the terminal phase of a trajectory, the needle was prone to minor buckling, even with the guide mechanism in place. This may have resulted in tip deflection or inaccurate insertion lengths.
- f) **Referencing errors:** As stated previously, needle tracking was hampered by noise, often caused by the folds on gelatine appearing as high-intensity regions on thresholding. This was particularly problematic for tip tracking in the *XY* plane as the needle was placed deeper in the phantom, making it less visible.

5. Discussion

5.1. High level performance analysis

This work describes the development and evaluation of an integrated robotic system for EUS-FNA/FNB. The system combines a 4 DoF TDCR endoscope, a 2 DoF bevel tip steerable needle guidewire platform and a DRL needle navigation planner, covering all aspects of the clinical workflow.

Current practice using manual endoscopes and straight needles is inherently constrained by limited reach and manipulability; our concept has the potential to provide clinicians with unprecedented multi-DoF control inside the liver, expanding the possible target areas from only the left lobe to deep seated lesions in the right and caudate lobe, as well as those surrounded by complex anatomy.

For a proof-of-concept, our TDCR and needle stages show satisfactory accuracy. The TDCR achieved bending ranges comparable to clinical gastrosopes (although the bending angles have not been explicitly quantified). FABRIKc was proven as an effective IK solver for our design. Experimental testing of the endoscope using the NDI Aurora magnetic system resulting in mean positional errors in the range of 20 mm. Grid sampling demonstrated its ability to reach points within a dome like workspace. Execution of the circular trajectory theoretically proved the ability to move freely within an insufflated stomach. The NeedleNav algorithm was able to converge to obstacle avoidance trajectories in ~ 2500 episodes within a margin of 3 mm around the target. Since the focus of this work was the physical robotic system, detailed evaluation of NeedleNav with tighter curvatures and more obstacles has not been reported. Preliminary testing has, however, been successful up to six independent obstacles, which points

to the generalisability of the model to more complex environments. Testing of the steerable needle validated our control policy and our notching technique to increase curvature. In phantom testing achieved errors also in the range of 20 mm , with a percentage error of $\sim 15\%$. Naturally, clinical implementation will require far smaller Euclidean errors and higher repeatability. While tip accuracy of clinically deployed endoscopic robots has not been reported previously, for reference, the Da Vinci Xi surgical robot has been reported to have submillimetre tip position error.^{43,44} The KUKA LBR Med, licensed for use in medical applications, has a repeatability of $\sim 0.1\text{ mm}$.⁴⁵ Hard tissue spinal robotic systems have a reported accuracy of $< 2\text{ mm}$.⁴⁶

Apart with greater access to lesions, this system will have significant implications for the clinical workflow of EUS-FNA/FNB. Dependence on operator skill and training times will be reduced. Standardisation of outcomes across centres will increase and the reliance on percutaneous and trans-jugular approaches will decrease. As with comparable level 3 autonomous systems such as Aquablation (Procept BioRobotics, California, USA), the operator's role (for the part of the procedure within the liver) will become supervisory, involving defining of the target, selecting potential trajectories and actively monitoring software and US imaging.⁴⁷

While these prospects are encouraging, several technical challenges, and correspondingly, directions for future work, remain.

5.2. Limitations and directions for future work

Firstly, the concept of bevel tip steering depends on a constant curvature assumption, which requires uniform stiffness of tissue. However, the liver is non-homogenous – particularly in this scenario, pathological livers will have variable regions of fibrotic or necrosed tissue with higher stiffness compared to healthy liver. Tissue is also displaced due to natural body movement (i.e. during breathing). This will result in a steadily increasing inaccuracy as the needle drifts from its predicted curvature trajectory. Thus, some form of feedback control will be needed, based on imaging or shape sensing techniques, where sections of the needle trajectory are actively sampled to detect and compensate for changing curvature/error. This may be US based, with embedded piezoelectric elements to increase needle visibility, or via shape sensing through an integrated fibre bragg grating (FBG). Indeed, several groups have combined imaging feedback with continuous control of needle rotation to achieve variable curvature and correct deviations. Abayazid et al. (2013) placed four sets of three FBGs along a 1 mm NiTi bevel tip needle and reconstructed its shape, curvature and bending plane to continuously measure and correct deviation of the z axis projection vector from a target region. Phantom experiments achieved $\sim 1.3\text{ mm}$ tip accuracy. Patel et al. (2015) continuously tracked a bevel tip needle's z axis projection vector and needle-to-target vector on MRI and passed the angular deviation to a closed loop controller for duty cycled modulation of needle rotation.⁴⁹ The team achieved a mean tip position error of 2.5 mm in a gelatine phantom. Fallahi et al. (2017) tracked needle tip position using 3D US and measured deviation in the x and y direction

relative to two sliding surfaces.⁵⁰ Errors were fed to a binary corrective controller (needle deviates to the right of the surface = curve left to compensate) to change the torsion angle. Experiments in gelatine phantom demonstrated an MAE of $\sim 0.5\text{ mm}$.

Secondly, the needle curvature must be increased. Although measurable deflection was observed, the curvature is presently insufficient for a complex obstacle avoidance task. Methods to augment curvature have already been discussed in section 2. For this project, a potential future strategy might be using advanced NiTi fabrication techniques such as water or cutting to create a pattern over the complete length of the needle. This will ensure a uniform and tighter curvature.

Thirdly, the mechanical reasons for error discussed in section 4 must be addressed. The TDCR in its present form is underactuated for a position and orientation control task. However, in actual clinical practice, an additional translational DoF will be added, giving it 5 total DoF and permitting a position and orientation control task. Tendon friction should be reduced through the integration of low friction steel bushings in all spacer discs. Steel tendons may be replaced by NiTi to eliminate errors from frayed wires. A pre-tensioning algorithm and tendon force/torque sensors should be introduced to eliminate slack in all tendons at zero position. The inverse kinematic framework must also be updated to account for changes in distal tendon length due to proximal segment curvature.

Finally, in its current form, NeedleNav cannot account for variable curvature. The key challenge here is to combine tip tracking information (introduced above) with the control policy, allowing the agent to actively adapt its short-term actions based on the instantaneous curvature returned by the tracking and compensation algorithm. NeedleNav is not generalisable post training – it learns a single reward maximising policy and cannot reach new targets or use variable curvatures. To overcome this, future iterations of the algorithm will require training in noisy environments using domain randomisation or uncertainty aware models.⁵¹ The workflow would involve pre-training a policy on patient specific anatomy while accounting for various needle behaviour and then deploying this trained policy with active curvature estimates to adapt action space vectors dynamically.

5.3. Steps toward clinical application

Although the system designed is proof-of concept, steps toward clinical deployment can be envisioned. The first step will be to move from gelatine phantoms towards animal liver, typically porcine models. Testing in perfused animal liver will provide key insights into needle performance in tissue regions with varying stiffness and trackability via US imaging. Eventually, testing should transition to *in vivo* animal studies to evaluate the clinical workflow under realistic conditions with respiratory and cardiac movement. The final pre-human trials will involve extensive cadaveric evaluation to train and familiarise clinicians with the system and measure accuracy in adult human livers.

A complete re-design of the system will be required, using biocompatible surgical grade components that are durable and sterilisable. The TDCR structure will need to accommodate additional channels for imaging, suction and water jets. ISO and IEC compliant electronics, servos, software and fail-safe systems will need to be integrated.⁵² A joystick-based control device could be used for manipulation of the TDCR distal endoscope section once it has been manually inserted into the stomach. The semi-autonomous needle platform will require an intuitive user interface for operators, allowing them to define targets, view, modify and select trajectories and monitor progress with the ability to take over if there are critical events during the procedure.

Any clinically deployed system will go through thorough regulatory pathways. Taking the regulatory framework in the United States as an example, as a novel, first-in-class semi-autonomous system for EUS needle interventions, this system will require clearance under the FDA's De-Novo pathway, subject to more stringent oversight compared to predicate-based 510(k) approvals. Initial clinical evaluation will proceed under an investigational device exemption, allowing for limited trials to assess safety and outcomes before pre-market approval.

6. Conclusion

This project introduced a proof-of-concept robotic platform that combines a TDCR, steerable bevel tip needle and a DRL path planner for EUS-FNA/FNB. The TDCR was designed by connecting a series of spacer discs in an interlocking fashion with a large central bore for the spring backbone and peripheral channels for the steel wire actuating tendons. Tendons were tensioned by six pulley-servo pairs. The DRL planner, NeedleNav, was designed as an online, off-policy entropy weighted soft actor critic with clipped double Q critics. The notched steerable needle was fabricated with sandpaper and diamond file and actuated by a rotational servo mounted on a translational rack-pinion mechanism. The TDCR and needle achieved a Euclidean MAE of ~20 and ~22 mm respectively. Evaluation validated the control policy for both stages, confirming the feasibility of a semi-autonomous system that improves lesion accessibility, accuracy of targeting, reduced operator dependence, better ergonomics and standardisation of outcomes. While results are promising, there are several directions for future work, including the integration of tip-tracking capability and variable curvature control, increasing the curvature of the needle using advanced machining techniques and improving the accuracy of the TDCR through friction reduction and pre-tensioning. The end goal is to reduce the error to clinically acceptable levels, which would likely lie at < 2 mm for the endoscope and < 1 mm for the needle.

References

1. Devarbhavi H, Asrani SK, Arab JP, Nartey YA, Pose E, Kamath PS. Global burden of liver disease: 2023 update. *Journal of Hepatology*. 2023 Aug;79(2):516–37. doi:10.1016/j.jhep.2023.03.017
2. Neuberger J, Patel J, Caldwell H, Davies S, Hebditch V, Hollywood C, et al. Guidelines on the use of liver biopsy in clinical practice from the British Society of Gastroenterology, the Royal College of Radiologists and the Royal College of Pathology. *Gut*. 2020 May 28;69(8):1382–403. doi:10.1136/gutjnl-2020-321299
3. Cholongitas E, Quaglia A, Samonakis D, Senzolo M, Triantos C, Patch D, et al. Transjugular liver biopsy: How good is it for accurate histological interpretation? *Gut*. 2006 Dec 1;55(12):1789–94. doi:10.1136/gut.2005.090415
4. Ramai D, Pannu V, Facciorusso A, Dhindsa B, Heaton J, Ofosu A, et al. Advances in endoscopic ultrasound (EUS)-guided liver biopsy. *Diagnostics*. 2023 Feb 19;13(4):784. doi:10.3390/diagnostics13040784
5. ICHIM VA, CHIRA RI, NAGY GA, CHIRAA, MIRCEA PA. Endoscopic ultrasound-guided biopsy of liver tumors. *In Vivo*. 2022;36(2):890–7. doi:10.21873/invivo.12778
6. Patel HK, Therapondos G, Galliano G, Romero Ricardo, Evans J, Cohen A, et al. Endoscopic ultrasound-guided liver biopsy using newer 19g FNB needles compared to percutaneous and transjugular liver biopsy: A tertiary center experience. *Techniques and Innovations in Gastrointestinal Endoscopy*. 2022;24(2):127–35. doi:10.1016/j.tige.2021.11.009
7. Rancatore G, Ligresti D, Rizzo GE, Carrozza L, Traina M, Tarantino I. Endoscopic ultrasound-guided fine needle biopsy of focal liver lesions: An effective mini-invasive alternative to the percutaneous approach. *Diagnostics*. 2024 Jun 24;14(13):1336. doi:10.3390/diagnostics14131336
8. Tantău A, Sutac C, Pop A, Tantău M. Endoscopic ultrasound-guided tissue acquisition for the diagnosis of focal liver lesion. *World Journal of Radiology*. 2024 Apr 28;16(4):72–81. doi:10.4329/wjr.v16.i4.72
9. Mok SR, Diehl DL. The role of eus in liver biopsy. *Current Gastroenterology Reports*. 2019 Jan 31;21(2). doi:10.1007/s11894-019-0675-8
10. Russo M, Sadati SM, Dong X, Mohammad A, Walker ID, Bergeles C, et al. Continuum robots: An overview. *Advanced Intelligent Systems*. 2023 Mar 23;5(5). doi:10.1002/aisy.202200367
11. Salkowski M, Checcucci E, Chow AK, Rogers CC, Adbollah F, Liatsikos E, et al. New Multiport Robotic Surgical Systems: A comprehensive literature review of Clinical Outcomes in urology. *Therapeutic Advances in Urology*. 2023 Jan;15. doi:10.1177/17562872231177781
12. Kato T, Okumura I, Song S-E, Golby AJ, Hata N. Tendon-driven continuum robot for endoscopic surgery: Preclinical development and validation of a tension propagation model.

IEEE/ASME Transactions on Mechatronics. 2015 Oct;20(5):2252–63.
doi:10.1109/tmech.2014.2372635

13. Kim Y, Cheng SS, Desai JP. Active stiffness tuning of a spring-based continuum robot for MRI-guided neurosurgery. *IEEE Transactions on Robotics*. 2018 Feb;34(1):18–28. doi:10.1109/tro.2017.2750692
14. Zhang Y, Sun H, Jia Y, Huang D, Li R, Mao Z, et al. A continuum robot with contractible and Extensible Length for Neurosurgery. 2018 IEEE 14th International Conference on Control and Automation (ICCA). 2018 Jun;1150–5. doi:10.1109/icca.2018.8444220
15. Dragone D, Donadio FF, Mirabelli C, Cosentino C, Amato F, Zaffino P, et al. Design and experimental validation of a 3D-printed embedded-sensing continuum robot for Neurosurgery. *Micromachines*. 2023 Sept 6;14(9):1743. doi:10.3390/mi14091743
16. Zhang X, Li W, Chiu PW, Li Z. A novel flexible robotic endoscope with constrained tendon-driven continuum mechanism. *IEEE Robotics and Automation Letters*. 2020 Apr;5(2):1366–72. doi:10.1109/lra.2020.2967737
17. Wang F, Wang H, Luo J, Kang X, Yu H, Lu H, et al. Fiora : A flexible tendon-driven continuum manipulator for laparoscopic surgery. *IEEE Robotics and Automation Letters*. 2022 Apr;7(2):1166–73. doi:10.1109/lra.2021.3134276
18. Amanov E, Nguyen T-D, Burgner-Kahrs J. Tendon-driven continuum robots with extensible sections—a model-based evaluation of path-following motions. *The International Journal of Robotics Research*. 2019 Nov 17;40(1):7–23. doi:10.1177/0278364919886047
19. Rox M, Esser DS, Smith ME, Ertop TE, Emerson M, Maldonado F, et al. Toward continuum robot tentacles for lung interventions: Exploring folding support disks. *IEEE Robotics and Automation Letters*. 2023 Jun;8(6):3494–501. doi:10.1109/lra.2023.3267006
20. Hong W, Zhou Y, Cao Y, Feng F, Liu Z, Li K, et al. Development and validation of a two-segment continuum robot for maxillary sinus surgery. *The International Journal of Medical Robotics and Computer Assisted Surgery*. 2021 Oct 20;18(1). doi:10.1002/rcs.2340
21. Feng F, Zhou Y, Hong W, Li K, Xie L. Development and experiments of a continuum robotic system for transoral laryngeal surgery. *International Journal of Computer Assisted Radiology and Surgery*. 2022 Jan 13;17(3):497–505. doi:10.1007/s11548-022-02558-7
22. Dupont PE, Simaan N, Choset H, Rucker C. Continuum Robots for medical interventions. *Proceedings of the IEEE*. 2022 Jul;110(7):847–70. doi:10.1109/jproc.2022.3141338
23. de Jong TL, van de Berg N, Tas L, Moelker A, Dankelman J, van den Dobbelaar J. Needle placement errors: Do we need steerable needles in interventional radiology? *Medical Devices: Evidence and Research*. 2018 Aug;Volume 11:259–65. doi:10.2147/mder.s160444
24. Van De Berg NJ. Needle steering mechanics and design cases [thesis]. Tu Delft; 2016.

25. Webster RJ, Kim JS, Cowan NJ, Chirikjian GS, Okamura AM. Nonholonomic modeling of Needle Steering. *The International Journal of Robotics Research*. 2006 May;25(5–6):509–25. doi:10.1177/0278364906065388
26. Misra S, Reed KB, Schafer BW, Ramesh KT, Okamura AM. Mechanics of flexible needles robotically steered through soft tissue. *The International Journal of Robotics Research*. 2010 Jun 3;29(13):1640–60. doi:10.1177/0278364910369714
27. Reed K, Majewicz A, Kallem V, Alterovitz R, Goldberg K, Cowan N, et al. Robot-assisted needle steering. *IEEE Robotics & Automation Magazine*. 2011 Dec;18(4):35–46. doi:10.1109/mra.2011.942997
28. Khadem M, Rossa C, Usmani N, Sloboda RS, Tavakoli M. Robotic-assisted needle steering around anatomical obstacles using notched steerable needles. *IEEE Journal of Biomedical and Health Informatics*. 2018 Nov;22(6):1917–28. doi:10.1109/jbhi.2017.2780192
29. Rox M, Emerson M, Ertop TE, Fried I, Fu M, Hoelscher J, et al. Decoupling steerability from diameter: Helical dovetail laser patterning for steerable needles. *IEEE Access*. 2020;8:181411–9. doi:10.1109/access.2020.3028374
30. Huang Y, Yu L, Zhang F. A survey on puncture models and path planning algorithms of bevel-tipped flexible needles. *Heliyon*. 2024 Feb;10(3). doi:10.1016/j.heliyon.2024.e25002
31. Lin J, Huang Z, Zhu T, Leng J, Huang K. Deep reinforcement learning-based robotic puncturing path planning of Flexible Needle. *Processes*. 2024 Dec 12;12(12):2852. doi:10.3390/pr12122852
32. Lee Y, Tan X, Chng C-B, Chui C-K. Simulation of robot-assisted flexible needle insertion using deep Q-Network. *2019 IEEE International Conference on Systems, Man and Cybernetics (SMC)*. 2019 Oct;342–6. doi:10.1109/smci.2019.8914191
33. Tan X, Lee Y, Chng C-B, Lim K-B, Chui C-K. Robot-assisted flexible needle insertion using universal distributional deep reinforcement learning. *International Journal of Computer Assisted Radiology and Surgery*. 2019 Nov 25;15(2):341–9. doi:10.1007/s11548-019-02098-7
34. Hu W, Jiang H, Wang M. Flexible needle puncture path planning for liver tumors based on deep reinforcement learning. *Physics in Medicine & Biology*. 2022 Sept 26;67(19):195008. doi:10.1088/1361-6560/ac8fdd
35. Haarnoja T, Zhou A, Abbeel P, Levine S. Soft actor-critic: Off-policy maximum entropy deep reinforcement learning with a stochastic actor. *International conference on machine learning* 2018 Jul 3 (pp. 1861–1870). Pmlr.
36. Rozeboom E, Reilink R, Schwartz M, Fockens P, Broeders I. Evaluation of the tip-bending response in clinically used endoscopes. *Endoscopy International Open*. 2016 Mar 30;04(04). doi:10.1055/s-0042-104115

37. Zhang W, Yang Z, Dong T, Xu K. FABRIKc: An efficient iterative inverse kinematics solver for continuum robots. 2018 IEEE/ASME International Conference on Advanced Intelligent Mechatronics (AIM). 2018 Jul;346–52. doi:10.1109/aim.2018.8452693
38. Webster RJ, Jones BA. Design and kinematic modeling of Constant Curvature Continuum Robots: A Review. *The International Journal of Robotics Research*. 2010 Jun 10;29(13):1661–83. doi:10.1177/0278364910368147
39. U.S. Food and Drug Administration. K182188: Ion Endoluminal System; Flexision Biopsy Needle—510(k) summary. Silver Spring (MD): FDA; 2019 Jan 14 [cited 2025 Aug 29]. Available from: https://www.accessdata.fda.gov/cdrh_docs/pdf18/K182188.pdf
40. Corpechot C, Gaouar F, El Naggar A, Kemgang A, Wendum D, Poupon R, et al. Baseline values and changes in liver stiffness measured by transient elastography are associated with severity of fibrosis and outcomes of patients with primary sclerosing cholangitis. *Gastroenterology*. 2014 Apr;146(4). doi:10.1053/j.gastro.2013.12.030
41. Archer AJ, Belfield KJ, Orr JG, Gordon FH, Abeysekera KW. EASL clinical practice guidelines: Non-invasive liver tests for evaluation of liver disease severity and prognosis. *Frontline Gastroenterology*. 2022 Feb 15;13(5):436–9. doi:10.1136/flgastro-2021-102064
42. Eyberg C, Karstensen L, Pusch T, Horsch J, Langejürgen J. A ros2-based testbed environment for Endovascular Robotic Systems. *Current Directions in Biomedical Engineering*. 2022 Jul 1;8(1):89–92. doi:10.1515/cdbme-2022-0023
43. Kwartowitz DM, Herrell SD, Galloway RL. Toward image-guided robotic surgery: Determining intrinsic accuracy of the Da Vinci Robot. *International Journal of Computer Assisted Radiology and Surgery*. 2006 Oct 11;1(3):157–65. doi:10.1007/s11548-006-0047-3
44. Ferguson JM, Pitt B, Kuntz A, Granna J, Kavoussi NL, Nimmagadda N, et al. Comparing the accuracy of the da vinci XI and da vinci SI for image guidance and automation. *The International Journal of Medical Robotics and Computer Assisted Surgery*. 2020 Sept;16(6):1–10. doi:10.1002/rcs.2149
45. LBR MED medical robot: Sensitive, precise, safe [Internet]. [cited 2025 Aug 29]. Available from: <https://www.kuka.com/en-us/industries/robots-used-in-medicine/kuka-solutions-for-medical-robots/lbr-med-medical-robot>
46. Benech CA, Perez R, Benech F, Shirk T, Bucklen BS. A quantitative accuracy assessment of the use of a rigid robotic arm in navigated placement of 726 pedicle screws. *BMC Surgery*. 2022 Nov 10;22(1). doi:10.1186/s12893-022-01838-y
47. Khanna R, Raison N, Granados Martinez A, Ourselin S, Montorsi F, Briganti A, et al. At The Cutting Edge: The potential of autonomous surgery and challenges faced. *BMJ Surgery, Interventions, & Health Technologies*. 2025 Mar;7(1). doi:10.1136/bmjsit-2024-000338
48. Abayazid M, Kemp M, Misra S. 3D flexible needle steering in soft-tissue phantoms using fiber Bragg grating sensors. 2013 IEEE International Conference on Robotics and Automation. 2013 May;5843–9. doi:10.1109/icra.2013.6631418

49. Patel NA, van Katwijk T, Gang Li, Moreira P, Weijian Shang, Misra S, et al. Closed-loop asymmetric-tip needle steering under continuous intraoperative MRI guidance. 2015 37th Annual International Conference of the IEEE Engineering in Medicine and Biology Society (EMBC). 2015 Aug;4869–74. doi:10.1109/embc.2015.7319484
50. Fallahi B, Rossa C, Sloboda RS, Usmani N, Tavakoli M. Sliding-based image-guided 3D needle steering in soft tissue. Control Engineering Practice. 2017 Jun;63:34–43. doi:10.1016/j.conengprac.2017.04.001
51. Tobin J, Fong R, Ray A, Schneider J, Zaremba W, Abbeel P. Domain randomization for transferring deep neural networks from simulation to the Real World. 2017 IEEE/RSJ International Conference on Intelligent Robots and Systems (IROS). 2017 Sept;23–30. doi:10.1109/iros.2017.8202133
52. Chinzei K. Safety of Surgical Robots and IEC 80601-2-77: The First International Standard for Surgical Robots. Acta Polytechnica Hungarica. 2019;16(8).
53. Center for Devices and Radiological Health. De Novo Classification Request [Internet]. FDA; [cited 2025 Aug 29]. Available from: <https://www.fda.gov/medical-devices/premarket-submissions-selecting-and-preparing-correct-submission/de-novo-classification-request>